ABSTRACT

Title of Dissertation: PHYSICS AND APPLICATIONS OF EXTENDED AIR HEATING BY FEMTOSECOND LASER FILAMENTATION

Ilia Larkin, Doctor of Philosophy, 2022

Dissertation directed by: Professor Howard Milchberg
Department of Physics

Femtosecond laser pulses of sufficient energy can propagate as filaments in air due to a dynamic interplay between nonlinear self-focusing and ionization-induced defocusing. A filament in air is characterized by a narrow, 100 μm diameter core propagating at high intensity for many Rayleigh ranges corresponding to the core diameter, surrounded by a lower intensity reservoir that exchanges optical energy with the core. The high intensity core ionizes the air and excites molecular rotational wavepackets in N_2 and O_2. Thermal relaxation of these excitations leads to air heating over very long and narrow volumes, launching acoustic waves and imprinting density profiles in air. These features enable longitudinal mapping of energy absorption, interaction with aerosols in air, guiding of high voltage discharges, and the generation of long air waveguides for subsequent laser pulses. All of these topics are detailed in this dissertation.

In particular, we present: (1) Single shot axially resolved energy deposition measurements, using a synchronized array of microphones, to see on a shot-by-shot basis the effect of air turbulence on nonlinear pulse propagation. (2) Measurements of the pre-breakdown evolution of a laser triggered high voltage spark gap, induced by a density channel imprinted by femtosecond laser pulses. By interferometrically measuring air heating and current leakage through the spark gap we clarify the role of laser plasma vs laser air heating in triggering breakdowns. (3) Air waveguiding experiments extended to ranges up to 50 m from the original ~1 m experiments. (4) Fog droplet clearing experiments showing that in natural filamentation of a collimated beam, direct optical interactions are the dominant clearing mechanism rather than acoustic effects.

PHYSICS AND APPLICATIONS OF EXTENDED AIR HEATING BY FEMTOSECOND LASER FILAMENTATION

by

Ilia Larkin

Dissertation submitted to the Faculty of the Graduate School of the
University of Maryland, College Park, in partial fulfillment
of the requirements for the degree of
Doctor of Philosophy
2022

Advisory Committee:
Professor Howard Milchberg, Chair
Professor Phillip Sprangle
Professor Kiyong Kim
Dr. Jared Wahlstrand
Dr. Eric Rosenthal

Dedication

To all the other Dr. Larkins, especially my grandfather Dr. A. I. Larkin.

Acknowledgements

The work presented in the thesis would not be possible without the help of numerous amazing individuals. First and foremost, I must thank Professor Howard Milchberg for providing me with the opportunity to do such great work in his lab and for helping me revise/edit my writing to present the science in a clear and concise manner. He somehow finds time to stop by and chat with each individual student at least once a week despite running a research lab now spread over four rooms and six different laser systems.

Next, I must thank all the numerous students past and present who have helped me over the years. The two former students who had the most impact on me are Dr. Eric Rosenthal and Dr. Nihal Jhajj. They taught me nearly everything I know about lasers and showed me two very different techniques for designing experiments. Eric showed me that occasionally its faster to just experimentally test something rather than figuring out if it will work or not. Nihal taught me that in other situations a five minute simulations can save your hours of fruitless work by proving that your goal is impossible. Dr. George Hine and Dr. Andy Goers also deserve a special thanks for approaching me when I was visiting as a prospective student and convincing me to tour and later join the lab.

As I have moved toward the end of my graduate student career I have been joined by Andrew Goffin and Andrew Tartaro who will carry on the filamentation research once I leave. Both have been a great help in the lab, Andrew G. has become our local nonlinear simulation expert and I leave my 10 TW laser in the talented hands of Andrew T. For our long-range propagation experiments I am also grateful

for the help provided by our collaborators at the Army Research Lab, Dr. Anthony Valenzuela and Dr. Aaron Schweinsberg. Tony especially has provided me with great advice both for experimental design and everything else in life. Jesse Griff-McMahon, a former undergrad in our lab deserves a shout out for asking me lots of complicated physics questions which led to numerous enlightening discussions. He also laid the foundations of YAPPE, our nonlinear simulation code. Thomas Produit and Malte Schroeder visiting from the research group of J. P. Wolf in the University of Geneva, Switzerland, made a great team with Eric and I as we powered through several late nights of data taking.

All the other graduate students who I haven't collaborated with directly still had a large impact on me. Dr. Bo Miao and Dr. Sina Zahedpour were always around to give me useful advice. Scott Hancock was an endless source of fun conversations covering everything from baking to bike repairs. Manh (Matthew) Le and Lucas Railing really highlighted that I was now a senior grad student by constantly coming to me for advice. Dr. Daniel Woodbury, Dr. Linus Feder, Dr. Robert Schwartz, Dr. Fatholah Salehi, Jaron Shrock, and Stefan Waczynski have also all contributed to making the lab a very friendly and welcoming work environment.

I also need to thank the many members of the IREAP staff who were essential to our research. Nolan Ballew taught me both the fast way and the correct way to make whatever part I needed in the machine shop with assistance from Jay Pyle and Tom Weimar. Nancy Boone, Taylor Prendergrast, and Dottie Brosius ensured that bureaucracy never slowed down our research when we needed to purchase something, travel for a conference, or get office supplies. Bryan Quinn, Don Schmadel, and

Shawn Fickes did their best to keep our old building functional despite all the holes we drilled in the walls and our best efforts to overload both the chilled water loop and the HVAC system. Josiland Chambers has also been a great help with academic advising and paperwork. Outside of UMD Joe Juenemann and Bob Letiecq have both been gone above and beyond their roles as laser service engineers and have essentially trained me in laser repair and maintenance by answering the numerous tech support requests I have sent their way.

Finally, thank you to my parents and sister who have done a great job ensuring I have a healthy work/life balance by either coming to visit or inviting me on vacation at least a few times a year. And a special thanks to an old friend from high school who stayed in touch throughout all these years and was always happy to chat.

Table of Contents

List of Figures

List of Abbreviations

LG – Laguerre Gaussian

NIR – Near Infrared

CPA – Chirped Pulse Amplification

SSSI – Single-shot Supercontinuum Spectral Interferometry

UPPE – Unidirectional Pulse Propagation Equation

LIBS – Laser Induced Breakdown Spectroscopy

FWHM – Full Width at Half Maximum

MPI – Multi-Photon Ionization

LIDAR – Light Detection and Ranging

TFP – Thin Film Polarizer

CCD – Charge Coupled Device

A/D – Analog/Digital

FPGA – Field Programable Gate Array

CW – Continuous Wave

GPU – Graphics Processing Unit

HEPA – High Efficiency Particulate Air (filter)

HV – High Voltage

RF – Radio Frequency

DC – Direct Current

TEM – Transverse Electro-Magnetic

Nd:YAG – Neodymium-doped Yttrium Alumina Garnet

CMOS – Complementary Metal Oxide Semiconductor

ILMI – Intense Laser Matter Interactions (lab)

Chapter 1: Introduction

1.1 Thesis outline

This dissertation will focus on work done in the part of the University of Maryland's Intense Laser Matter Interactions Lab focused on filamentation -- studying nonlinear propagation of ultrashort laser pulses in air. Previous works from the group have documented how energy deposited by a filament scales with laser parameters (energy, pulse duration) [1,2], the properties of the single-cycle acoustic wave produced by a filament [3], how air heating behaves as a function of repetition rate [4], how air heating can be increased by resonantly driving rotational excitations [5], and demonstrations of a short air waveguide using filament air heating [6,7]. The work presented here builds upon all of these foundations.

The first Chapter will motivate research into filamentation by reviewing important prior works, providing common applications, and discussing the relevant physical effects needed for filamentation. Chapter 2 presents single shot measurements of extended filament energy deposition highlighting the importance of air turbulence even in a controlled laboratory environment. Chapter 3 demonstrates how air heating from a filament, or heating using rotational excitation only, can be used to trigger high voltage spark gaps. The difference in spark properties with or without initial plasma present leads to a study of filament plasma evolution in the presence of a strong applied electric field. Chapter 4 demonstrates an improvement to previous air waveguide experiments by utilizing a multi-filamenting LG_{01} beam

profile. Guiding of a secondary laser beam is demonstrated over the length of a 40 m hallway. In Chapter 5, two additional experiments are briefly discussed regarding the use of filament energy deposition to clear fog. The first experiment shows that air heating using rotational excitations can be used to clear fog and the second is a controlled single droplet experiment to determine the physical mechanism behind the fog clearing.

1.2 Filamentation

Filamentation is a nonlinear propagation regime of high-power laser pulses in a transparent medium characterized by an intensity dependent refractive index which leads to self-focusing, overcomes diffraction, and is arrested by a different, higher intensity threshold, physical mechanism [8]. A NIR (near infrared) laser pulse filamenting in air propagates with a ~100 μm diameter high intensity core where self-focusing from the Kerr effect is balanced by diffraction and defocusing from plasma [9]. A surrounding lower intensity reservoir replenishes energy in the core sustaining it over distances much greater than the Rayleigh length of the core. This extended high intensity propagation leaves a corresponding narrow channel of heated air once plasma recombines and air thermalizes [1].

Early experimental study of filamentation began when long and thin damage tracks discovered within a glass sample after the focus of a pulsed laser were attributed to self-focusing [10]. The damage was caused by ionization within the solid medium but self-focusing correctly explained how intensity above the ionization threshold was maintained over long distances. Knowing the mechanism of self-

focusing, predictions were made for P_{crit}, the minimum power needed to overcome diffraction and form a filament [10] though recent works have criticized the concept of having a critical power since self-focusing strength varies strongly with pulse duration which is not conserved during nonlinear propagation [11]. For beams above the critical power early simulations were done to predict the distance needed for a laser pulse to collapse with or without an applied lens [12]. The simple equation provided by Marburger is still commonly used as a back-of-the-envelope approximation for determining necessary beam size and power for filament applications.

The critical power for filamentation with a Gaussian beam profile is given by [13]:

$$P_{crit} = \frac{3.79\,\lambda^2}{8\,\pi n_0 n_2} \tag{1.1}$$

In air, with an 800 nm laser, this is roughly 12 GW [14]. Since n_2, the nonlinear refractive index, scales with atomic density, critical power is decreased by more than three orders of magnitude in solids [15]. The technological breakthrough that allowed the study of filamentation in air was chirped pulse amplification (CPA) [16]. By using CPA with a broadband lasing medium such as titanium doped sapphire (Ti:Sapphire) energetic femtosecond pulses can be created. Modern turnkey laser systems can achieve ~5 mJ energies (~10 P_{crit}) and lasers in national labs are pushing beyond the 1 PW peak power limit at a 10 Hz repetition rate [17]. With the availability of such laser systems, filamentation could be studied in air with extended propagation lengths [18]. The Teramobile group built a mobile laser system and observed filamentation over hundreds of meters horizontally as well as recording plasma fluorescence from

many kilometers away vertically [19,20]. More recently researchers at the Naval Research Lab tested kilometer length filamentation in a controlled indoor environment with variable strength turbulence and numerous diagnostics [21].

With laser powers many times the critical power, many separate filaments are formed in a phenomenon termed multi-filamentation. These filaments are nucleated on local intensity maxima within a laser beam profile and the number of filaments scales with the number of critical powers [22]. For applications where control is needed over multi-filament positioning several approaches exist to localize individual filaments within the pulse. A simple wire mesh is capable of creating a regularized array of filaments [23] or a more robust structure can be created by an amplitude mask with widely spaced holes [24]. As will be demonstrated in Chapter 4 phase masks can be used to convert the laser mode to something other than a Gaussian as an alternative method for controlling the distribution of filaments. For applications where a single large filament is needed, pulsed $\lambda = 10.6$ μm CO_2 lasers have been recently developed with sufficient peak power to filament in air. The filament cores formed are nearly 1 cm in diameter, approximately 100× wider than those formed with a $\lambda = 800$ nm laser pulse [25].

In parallel with striving to generate ever longer and more intense filaments there has also been ongoing research into various phenomena associated with single filaments. One phenomenon is the wide spectral broadening of the initial laser pulse, generating a ‘supercontinuum’ and conical emission [26]. Spectral content of a femtosecond pulse propagating in atmosphere before and after filamentation as well as a full color photograph of a post-filament pulse is shown in Fig. 1.1 below.

Supercontinuum generated in a xenon gas cell by a filamenting 800 nm laser pulse can cover the entire visible range from 400 to 700 nm. This coherent white light source has been used extensively by our research group for the Single-shot Supercontinuum Spectral Interferometry (SSSI) measurement technique [27]. This technique allows measurement of laser intensity with femtosecond temporal resolution, or by using a pulse with known intensity the nonlinear coefficient, n_2, has been measured in multiple gases at a range of wavelengths [14]. Other recent works have used the broad bandwidth of supercontinuum generated in a hollow core fiber or a stack of glass plates to generate a nearly single-cycle pulse [28–30].

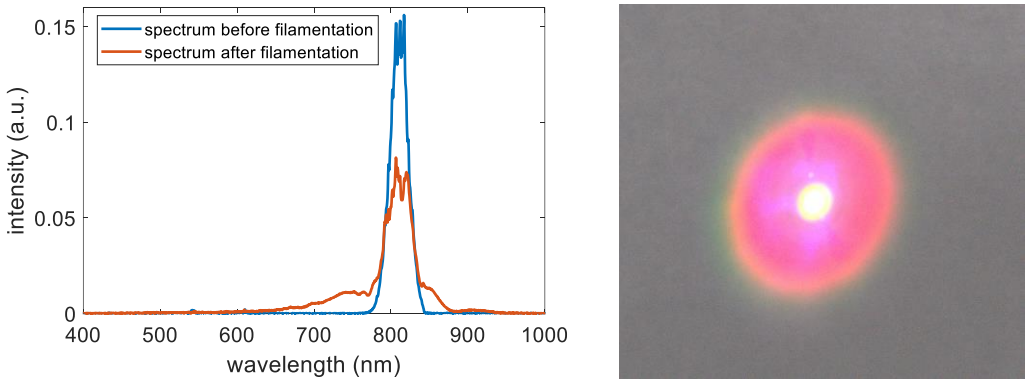

Figure 1.1 Left, laser spectrum before and after filamentation, normalized for equal integrated intensity. Right, photograph of a laser pulse after filamenting showing supercontinuum core.

One other area of interest in filamentation is the residual effect on the transparent medium through which the laser pulse propagates. Filaments in air deposit energy into the propagation medium primarily through plasma generation, the density of which depends on the focusing geometry [31]. The lifetime of such a plasma has recently been interferometrically measured to be less than 1 ns [32] and longitudinal extent of the plasma was directly measured with grazing angle interferometry [33]. Once a plasma generated by field ionization in a filament thermalizes and

recombines, the air is left instantaneously heated (on a timescale fast compared to the air hydrodynamics timescale of $a/c_s \sim 300$ ns, where $a \sim 100$ μm is the filament core diameter and $c_s \sim 300\ m/s$ is the air sound speed), generating a pressure spike that launches a single-cycle acoustic wave, whose amplitude is proportional to laser energy deposited per unit length [34]. For filaments, this single-cycle acoustic wave was directly observed using interferometry [3] and was used by our group to axially map filament energy deposition profiles by scanning a single microphone along the length of a filament [1]. The work in Chapter 2 further develops this experimental technique by using an array of microphones to record all spatial information in a single shot such that shot-to-shot details are not masked by averaging over laser power fluctuations or air turbulence. The work in Chapter 3 also relies on filament air heating, but compares the situation of a single filamenting pulse where heating is predominantly due to plasma to a train of eight pulses of lower intensity which heat air by resonantly exciting rotational states of air molecules [5].

In parallel with experimental advances, new high-fidelity, nonlinear laser pulse propagation simulations have been developed as well. The most common simulations are numerical solutions of either the nonlinear Schrödinger equation (NLSE) or the unidirectional pulse propagation equation (UPPE) [35]. Modern desktop computers have sufficient system memory for cylindrically symmetric simulations with 0.2 fs temporal resolution and 2 μm transverse resolution accurately modeling self-focusing, ionization, molecular rotations, and four wave mixing. A high-end server can handle full 3D simulations over hundreds of meters allowing the introduction of beam nonuniformities or air turbulence [36]. Simulations from the

Naval Research Lab have also focused on the air chemistry resulting from ionization [37] and have shown the strong effect turbulence has on self-focusing collapse location [38,39].

The nonlinear propagation of filaments has led to numerous applications. These applications take advantage of either spectral broadening and self-focusing experienced by the laser pulse itself, or energy deposition of the pulse into the air and subsequent hydrodynamic effects. Self-focusing allows laser induced breakdown spectroscopy (LIBS) [40], or other experiment that requires high intensity at a distance, to be performed hundreds of meters from the laser source without the use of large focusing optics. Air heating by a filament generates meter long narrow channels of heated air with sub-ambient density. A decrease in density corresponds to a lower breakdown voltage which has been used to successfully trigger high voltage spark gaps and is being investigated as a way to generate a 'laser lightning rod' [41]. Additionally, regions of air with lower density can also be used to steer light due to the lower refractive index. This has been used both to guide subsequent co-propagating laser pulses, and to collect remote signals [6,7]. To understand what applications filaments can be used for some knowledge is needed of the underlying physical mechanism, this will be discussed in the next section.

1.3 Physics of filamentation

1.3.1 Self-focusing

The self-focusing experienced by a high intensity laser pulse propagating through air is due to the Kerr effect. This is a nonlinear effect where the index of refraction has an intensity dependent component.

$$n_{eff} = n_0 + n_2 I \tag{1.2}$$

This comes about from the polarization becoming nonlinear in the electric field strength at high intensities. In air the second order $\chi^{(2)}$ term vanishes due to centrosymmetry, leading to:

$$\boldsymbol{P} = \varepsilon_0 \left(\chi^{(1)} + \frac{3}{4} \chi^{(3)} |\boldsymbol{E}_\omega|^2 \right) \boldsymbol{E}_\omega \tag{1.3}$$

This leads to an effective index of refraction

$$n_{eff} = \left(1 + \chi^{(1)} + \tfrac{3}{4} \chi^{(3)} |\boldsymbol{E}_\omega|^2 \right)^{1/2} \approx n_0 + \tfrac{3}{8 n_0} \chi^{(3)} |\boldsymbol{E}_\omega|^2 \tag{1.4}$$

which is commonly written as:

$$n_{eff} = n_0 + n_2 I \tag{1.5}$$

where intensity is given by:

$$I = c\, n_0 \varepsilon_0 \frac{|E(\omega)|^2}{2} \tag{1.6}$$

So that the nonlinear refractive index is related to $\chi^{(3)}$ by:

$$n_2 = \frac{3}{4 \varepsilon_0 c n_0^2} \chi^{(3)} \tag{1.7}$$

Here $n_2 \sim 8 \times 10^{-20}$ cm^2/ W [14] for $\lambda = 800$ nm in both N_2 and O_2. A 1 TW/cm^2 peak intensity laser pulse propagating over 1 m will have the highest intensity central region phase delayed by ~0.6 radians relative to the low intensity periphery of the beam. Because this produces a phase curvature similar to that applied by a focusing

lens, the laser beam will start focusing without any external optics. For low intensity beams this self-focusing is insufficient to overcome the defocusing caused by linear diffraction. The condition where diffraction is defeated by self-focusing leads to a critical power threshold

$$P_{crit} = \frac{3.79\,\lambda^2}{8\pi n_0 n_2} \tag{1.8}$$

The threshold is a power rather than an intensity criterion since both diffraction and self-focusing scale inversely with transverse beam area.

The self-focusing considered above results from the electronic nonlinear optical response of the medium's atoms and molecules and is nearly instantaneous compared to the ~50 fs pulse duration often used in filamentation experiments. A second temporally delayed effect results from the molecular rotational response and contributes even more significantly in air for laser pulses longer than 100 fs. Molecular vibrational responses also exist, but require a larger bandwidth than is used in this work and do not play a role [42]. The delayed nonlinear effect comes from molecular alignment of air constituents, namely O_2 and N_2 molecules. The air molecules have a non-isotropic polarizability with $\alpha_{\parallel}$ along the long axis of the molecule larger than the transverse polarizability $\alpha_{\perp}$. Under an applied electric field the molecules experience a torque which aligns them parallel to the electric field. Since the polarizability for each molecule increases once it becomes aligned, the laser pulse experiences an increase in susceptibility delayed by the time required for the molecules to become aligned. This is written in compact form as an effective delayed Kerr effect. Fig. 1.2 below shows the computed rotational $\chi^{(3)}$ demonstrating the increased overlap of $\chi^{(3)}$ and intensity at longer pulse durations.

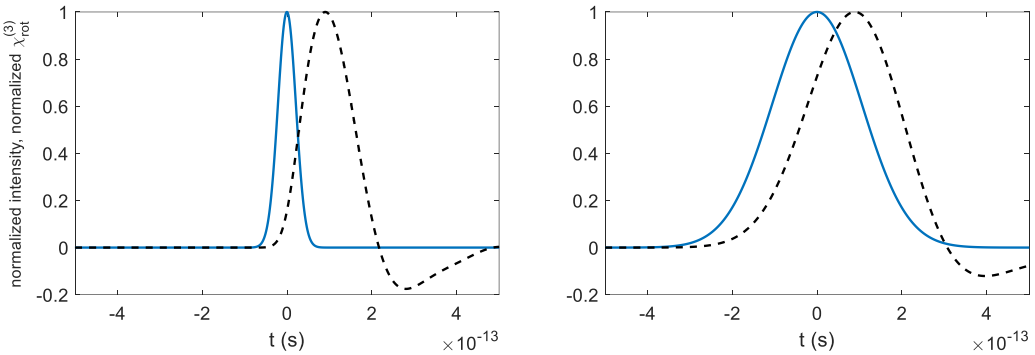

Figure 1.2 Rotational response for a 50fs (FWHM) and 250 fs pulse. Solid blue line indicates normalized temporal intensity profile, dashed black line indicates normalized rotational $\chi^{(3)}$ calculated using the density matrix approach detailed in previous works [43].

For an impulsive electric field, such as from a laser pulse, a range of molecular rotational states remain excited even after the laser pulse has propagated onwards. After a certain period, the molecules return into alignment, generating a 'rotational revival' when the susceptibility increases once more even though the laser pulse is long gone. At the time of these revivals the molecular rotations can be resonantly pumped by an additional laser pulse to efficiently deposit energy into the air. A full quantum mechanical derivation of the molecular rotational response to intense laser pulses is found in previous works from this research group [43,44].

1.3.2 Defocusing

A laser pulse undergoing self-focusing is in a runaway process characterized by shrinking beam size and increasing intensity. For a filament to form, a collapse arrest mechanism is needed. This mechanism must be a higher order function of intensity such that at low intensity self-focusing dominates, but above a clamping threshold the defocusing mechanism dominates forming a dynamic equilibrium. For NIR pulses in air, the physical mechanism of collapse arrest is ionization and

subsequent defocusing caused by the plasma. Substantial ionization of atmosphere occurs once the pulse intensity goes beyond ~50 TW/cm^2 [45].

Depending on laser wavelength and pulse duration different physical mechanisms dominate the ionization process of air constituents. For pulse durations longer than several picoseconds at NIR wavelengths avalanche ionization generates most of the free electrons [46]. This process relies on the presence of initial seed electrons which are accelerated by the laser electric field until their kinetic energy is sufficiently high to collisionally ionize other molecules. As the name implies, this process repeats when new electrons are generated leading to an 'avalanche' of ionization.

For generating the initial electrons in avalanche ionization or for shorter pulses tunneling ionization and MPI (multiphoton ionization) are the dominant mechanisms. In multiphoton ionization the energy of multiple photons is used to free an electron. For $\lambda = 800$ nm light with 1.55 eV per photon, 8 photons are needed to ionize an oxygen molecule (ionization potential 12 eV [47]), implying an ionization rate $\propto I^8$. Lower frequency lasers (with correspondingly lower photon energy) require more photons for MPI making the process less likely.

Tunneling ionization occurs when the laser electric field distorts the atomic potential sufficiently such that an electron has some probability to tunnel out of the bound state. This depends on the strength of the electric field rather than photon energy so the process stays relevant at lower frequencies. Whether tunneling or multiphoton ionization is dominant is quantified by the Keldysh Parameter γ [48].

$$\gamma = \omega\left(2m_e I_p\right)^{\frac{1}{2}}/(\,eE_0) \tag{1.9}$$

Where I_p is the ionization potential, E_0 and ω are the electric field amplitude and frequency, and m_e and e are the electron mass and charge. For $\gamma \ll 1$, tunneling ionization is the dominant mechanism, whereas for $\gamma \gg 1$, MPI dominates. For the $\lambda = 800$ nm laser beams in air at $I \sim 100$ TW/cm^2, which are used extensively in the experiments described later in this thesis, $\gamma \sim 1$, so that both tunneling and multi photon ionization play an important role.

Ionization of the medium through which the laser is propagating has several effects on the laser pulse. The simplest effect is that energy is lost from the laser pulse to ionize the medium. Additionally, a partially ionized medium has different optical properties compared to a unionized medium. The tail end of a laser pulse will experience a different refractive index due to plasma produced by the front of the pulse.

$$n_{plas} = \sqrt{1 - \frac{\omega_p^2}{\omega^2}} \tag{1.10}$$

$$\omega_p^2 = \frac{n_e e^2}{\varepsilon_0 m_e} \tag{1.11}$$

where ω_p is the plasma frequency and n_e is the electron density. This refractive index is always less than one, leading to a localized phase advance—causing beam divergence—when a portion of a laser pulse encounters either a pre-existing plasma or generates one.

1.3.3 Air response

All of the experiments presented in this dissertation utilize the long timescale hydrodynamic evolution of air after a filament. This is a brief primer on the timescale and magnitude of the various effects that follow an 800 nm filament in air. First there is a near instantaneous nonlinear response in air molecules that modifies the refractive index and leads to self-focusing. Nearly simultaneously photoionization is happening generating a peak plasma density $n_{e0} \sim 2 \times 10^{16}$ cm^{-3} for pulses with weak initial geometric focusing [33]. Delayed by approximately 100 fs is rotational alignment of air molecules further increasing the susceptibility in regions of high intensity [49]. Once the laser pulse is no longer present the molecules with excited rotational states experience rotational revivals on the picosecond timescale before collisionally decohering, repartitioning energy to translational states, thus heating the air [44]. Over the nanosecond timescale free electrons generated from ionization recombine, releasing energy as either remitted light or as thermal heating [32]. The energy deposited by a filament has been measured the range of 2—5 μJ / cm [1]. If this is assumed to be deposited into a 100 μm diameter cylinder and excites translational and rotational states of atmospheric density air molecules, then by $\Delta E = (5/2) N_0 k_B \Delta T$ we get a temperature increase of 30—75 °C. This air heating leads to local pressure increase in the air. As a result of pressure imbalance an acoustic wave is launched radially outwards on the time scale of $\tau = a / c_s$ where a is the filament core size and c_s is the speed of sound corresponding to $\tau \sim$ 300 ns [3]. This is a single-cycle acoustic wave with wavelength corresponding to the filament transverse size and amplitude proportional to the local energy deposited [1]. This wavelength corresponds to an acoustic frequency of ~3 MHz, but owing to its single-cycle nature

the wave covers the entire acoustic spectrum, occurring as a weak audible pop. Once pressure equilibrium is achieved with the surrounding air the heated region is still at lower density of about 98% of atmospheric after 100 μs [50]. The low density heated region dissipates based on the thermal diffusion rate, lasting for approximately 1 millisecond before dropping below the detection threshold [50]. For high repetition rate lasers this heated region is constantly replenished; an equilibrium is established with the heated air rising due to buoyancy [4]. For the work presented here a 10 Hz repetition rate laser is used allowing sufficient diffusion time so every pulse starts propagation through undisturbed air.

Chapter 2: Single-shot imaging of filament collapse in air turbulence

2.1 Introduction

The propagation of high peak power laser pulses through gases has applications spanning sub-millimeter scales for laser-driven relativistic electron acceleration [51] in thin gas jets to hundreds of meters in the atmosphere for applications in light detection and ranging (LIDAR) [52] and laser-induced breakdown spectroscopy (LIBS) [40]. In many cases, it is important to have a visualization of the full propagation path of the pulse in the gas. For long propagation ranges in the atmosphere, shot-to-shot variations from jitter in laser parameters and atmospheric fluctuations will lead to significant variations in the beam's transverse profile, axial energy deposition, trajectory, and collapse location [38,39,53–55].

In prior work, records of long (> few cm) propagation profiles have been experimentally determined in several ways. One method is intercepting the beam along the propagation path and then, via propagation simulations, inferring aspects of the pulse propagation history to the point of interception [56,57]. Each shot, however, is sensitive to fluctuations and has a different propagation evolution. For femtosecond filaments, one approach for single-shot imaging is to use the recombination radiation from plasma generation [56]. However, the huge field of view needed to capture the full filament path precludes resolving axial detail. Another method is shot-by-shot scanning of a miniature microphone along the propagation path [1] to pick up the single-cycle cylindrical acoustic wave launched locally [3,58]. The acoustic signal is

an excellent proxy for the local energy absorbed by the air, allowing a reconstruction of the laser pulse's axial energy deposition profile [1]. However, owing to unavoidable laser and air fluctuations, the full axial profile smooths over fluctuation-dependent details of interest when averaging many microphone traces at each position.

In this Chapter, we use a synchronized microphone array to record, in a single-shot, the full axial energy deposition profile in air of a high peak power femtosecond pulse. We examine pulses that undergo optical collapse and then propagate as filaments. Our method enables visualization of the shot-to-shot dependence of filamentary propagation on fluctuations in laser parameters and on turbulence-induced air fluctuations.

In air, pulse collapse occurs due to positive self-lensing from nonlinear electronic and rotational contributions to the effective refractive index from nitrogen and oxygen. Collapse is arrested when the local laser intensity reaches the threshold for ionization of oxygen, $I_{th} \sim 5 \times 10^{13}$ W/cm^2 [45], after which the interplay between self-focusing and plasma defocusing leads to a self-guided beam whose central portion propagates as a tight, $\sim 100\ \mu$m diameter "core" at intensity $\sim I_{th}$ surrounded by a lower intensity periphery [59]. Most well-known applications of filaments [6,40,52,60–62] rely on well-controlled and reproducible propagation.

A femtosecond air filament deposits energy into its generated plasma channel and into the excitation of molecular rotational wavepackets in N_2 and O_2 [2,5]. At each location along the filament path, the weakly ionized plasma recombines in less than ~10 ns [63], and the rotational excitation thermalizes on a ~100 ps timescale

[44], leading to a very fast local increase in the thermal energy (and pressure) of neutral air [64]. The rise time of this pressure spike is much faster than the acoustic response timescale of the filament-heated gas ($\tau_a \sim a / c_s \sim 150$ ns, where $a \sim 50\,\mu m$ is the filament core radius and $c_s \sim 3 \times 10^4$ cm/s is the sound speed in ambient air); the pressure spike drives an outwardly propagating single-cycle cylindrical acoustic wave [45,57] whose local axial amplitude is proportional to the local energy deposited. The peak in the acoustic signal registered by a microphone a distance r from the filament at the axial position z is $\Delta S_{mic}(z) \propto \Delta P(z)/\sqrt{r} \propto \Delta\epsilon(z)$, where $\Delta P(z)$ is the peak pressure amplitude of the acoustic wave and $\Delta\epsilon(z)$ is the laser energy per unit length absorbed at position z through plasma generation and excitation of molecular rotation [1]. For this to be an accurate local measurement the microphone aperture width should be $w < 2r$, and $r << L$, where L is the filament length.

2.2 Experiment

The experimental setup is shown in Fig. 2.1. Filaments were generated by 1-5 mJ pulses at central wavelength $\lambda = 800$ nm from a Ti:Sapphire laser system, with pulse width adjusted in the range 40-200 fs by changing the pulse compressor grating spacing. The pulse energy was finely controlled in advance of the compressor with a motor-controlled $\lambda/2$ plate and a thin film polarizer (TFP). The pulse was then passed through a vacuum spatial filter to generate a near-Gaussian mode, after which a small portion was directed to a CCD camera calibrated with a power meter to measure the energy on every shot. After pulse compression, the transmission through a 95/5 (R/T)

beamsplitter was sent to a single-shot autocorrelator to record the FWHM pulse duration on every shot, with the calibration adjusted for dispersion in the beamsplitter. The beam was then directed to a 4× down-collimating reflective telescope, with leakage from a dielectric turning mirror relay-imaged onto a Shack-Hartmann wavefront sensor (Imagine Optics HASO4 First) to determine the phase front curvature on every shot.

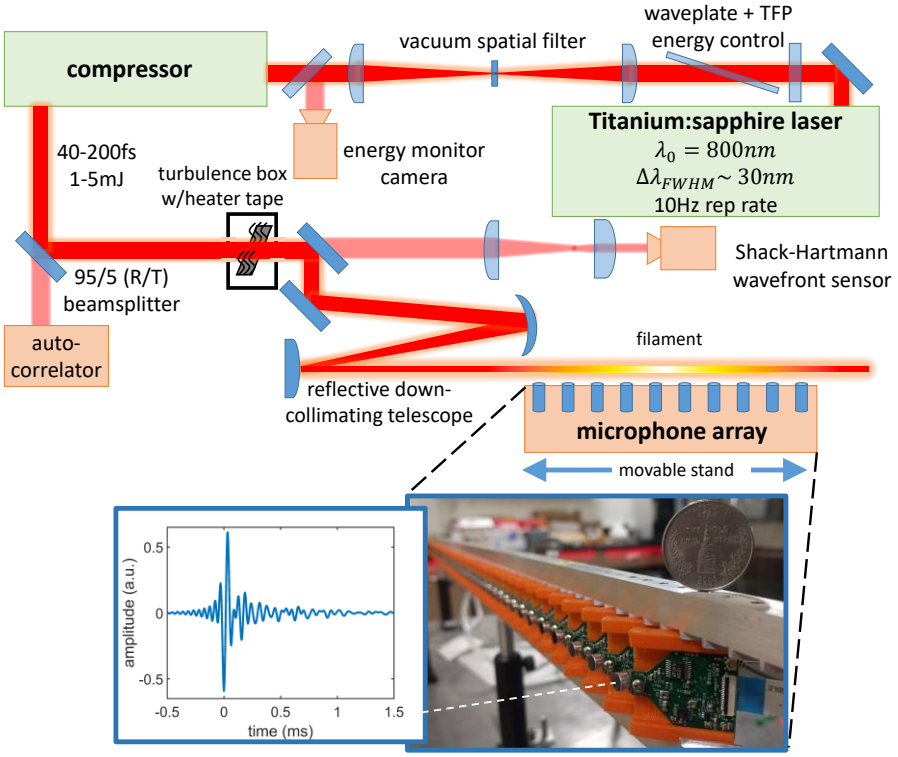

Figure 2.1 Top: Optical setup. Bottom: Microphone array and sample single microphone signal, with white dashed line pointing to single microphone. A quarter is shown in the microphone array photo for scale.

The collimated beam emerged from the telescope with $w_0 = 1.65$ mm ($1/e^2$ intensity radius) and propagated along a 5.5 m run until a beam dump at the end of the lab. The collapse was governed entirely by nonlinear phase accumulation in air without any assistance of linear beam focusing; even a weak lens can stabilize the collapse position, as shown later.

The microphone array was mounted on a mobile cart and aligned to be at a fixed radial position of ~3 mm from the filament. The array is composed of 64 miniature electret condenser microphones (Panasonic WM-61A) with aperture $w = 6$ mm, each mounted to a separate circuit board that does 24 bit A/D conversion at 44.1 kHz. The microphone, with a peak frequency response of ~20 kHz, registers the single-cycle acoustic wave (where $\tau_a{}^{-1} \sim 3$ MHz) as an impulse response. The microphones were mounted at 2 cm longitudinal spacing for a full span of 126 cm, providing sufficient axial resolution to capture details of the shot-to-shot variations along the full filament extent. The microphones are connected to a central hub with FPGA synchronization of the array and USB data transfer to a computer. Data was acquired continuously from the microphones and at 10 Hz from all other diagnostics.

2.3 Results

For a collimated beam that collapses and propagates as a filament, there can be large shot-to-shot fluctuations in the axial energy deposition profile. Fig. 2.2(a) compares a single-shot array trace, where each point corresponds to the peak of the microphone signal at that location (a sample microphone trace is shown in Fig. 2.1), to a trace averaged over 1000 shots at 10 Hz. The pulse propagates from left to right in the plots. The interval between shots is much greater than the ~ 2 ms needed for the air density to recover [1,60]. The error bars associated with the average are the $\pm$ standard deviations of the signals at each of the array microphones. The single-shot (red) trace shows a much sharper increase to its maximum than the average trace. This is because the single-shot trace has captured the onset of pulse collapse and

filamentation, whereas the average trace has smeared this region out. By contrast, Fig. 2.2(c) shows that even relatively weak assistance by a lens, here at $f/300$, greatly stabilizes the filament onset location on the left, where the single-shot and average curves largely track one another except for some deviation near the second hump of the curves. The error bars on the average curve are much smaller, in agreement with the single microphone axial scans of $f/600$ lens-assisted filaments in [1].

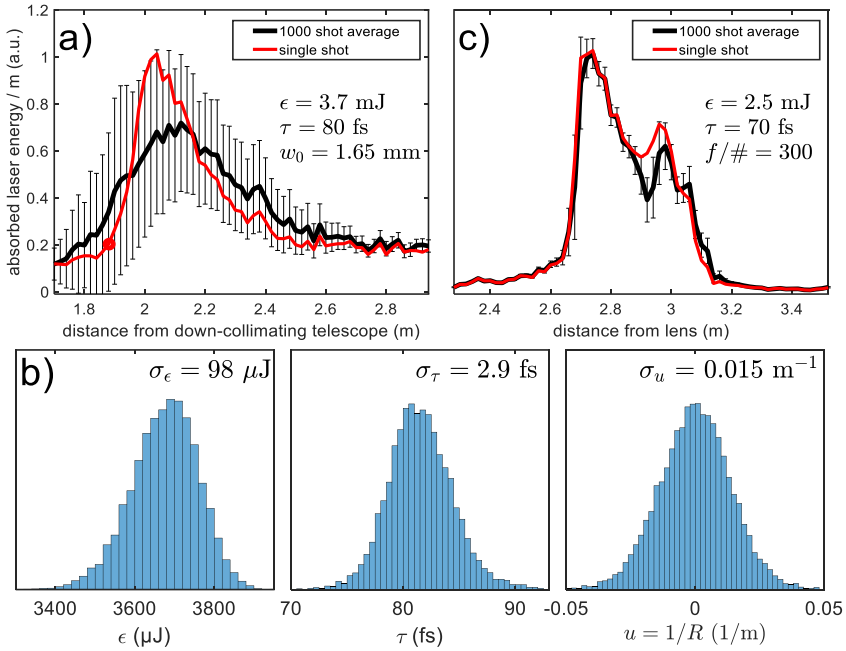

Figure 2.2 Microphone array signal from a single-shot (red curve) compared to a 1000 shot average (black curve). The pulse propagates left to right. Error bars associated with the average curves are the ± standard deviations of the signals at each microphone. **(a)** Filamentation with collimated beam. Laser: 3.7 mJ, 80 fs FWHM, $w_0 = 1.65\,mm$. **(b)** Histograms of pulse energy (ε), FWHM pulse duration (τ) and wavefront curvature ($u = 1/R$) over 10,000 shots, with standard deviations shown in the panels. **(c)** Lens-assisted filamentation at $f/300$. Laser: 2.5 mJ, 70 fs FWHM, $w_0 = 5\,mm$ incident on 3 m lens.

While the microphone array provides the energy deposition profile over the full filamentary propagation path, we now concentrate on the pulse collapse and filament onset location, as this is a measure of the path-integrated effect of the fluctuations leading to the shot-to-shot nonlinear propagation variations. These fluctuations are either intrinsic to the pulse (energy, pulse width, phase front) or

imposed on the pulse (phase front perturbations by externally supplied turbulence). To proceed, we define the collapse location as the axial position where energy deposition per unit length reaches 20% of its peak value. This location is marked as filled-in circle on the single-shot (red) trace in Fig. 2.2(a); 20% and higher gives very similar results, while thresholds as low as 10% result in some non-collapse locations being counted.

The intrinsic pulse fluctuations are measured, as shown in Fig. 2.1, with the pulse energy monitor (pulse energy ε), single-shot autocorrelator (pulse FWHM τ), and wavefront sensor (wavefront radius of curvature R). For the wavefront measurement we consider, as intrinsic to the laser, fluctuations measured at the down-collimating telescope. As discussed below, the wavefront fluctuations are from air turbulence over the $\sim$10 m propagation path from the spatial filter to the telescope, plus a much smaller contribution making it through the spatial filter from upstream in the laser system. The externally-imposed fluctuations are from controlled turbulence introduced into the beam by a length of heater tape enclosed at the base of a 15 cm × 15 cm box with an open top and small apertures for the laser beam to enter and exit ~6 cm above the tape. The turbulence box was positioned immediately preceding the reflective telescope, as shown in Fig. 2.1.

Turbulence strength was measured using a spatially filtered λ = 532 nm CW diode probe laser sampled at 10 Hz by the 1 ms electronic shutter of a CCD camera. Given uniform turbulence along a propagation distance L, the spatial deflection of a laser beam has the variance $\sigma^2 = 0.97\, {C_n}^2 D^{-1/3} L^3$ [65], where σ is the standard deviation of the beam centroid on a camera, D is the average FWHM beam diameter

(all in meters), and $C_n{}^2$ is the refractive index structure parameter. For propagation of the probe laser across the lab under typical conditions, with all laser power supplies (a heat source) running, we obtained $C_n{}^2 = 6.4 \times 10^{-14}\ \mathrm{m}^{-2/3}$.

For the fixed nominal laser parameters of Fig. 2.2(a) ($\varepsilon = 3.7$ mJ, $\tau = 80$ fs, and $w_0 = 1.65$ mm at the output of the down-collimating telescope) without the turbulence box, Fig. 2.2(b) shows histograms of the fluctuations over 10,000 shots, with the standard deviations σ_ε , σ_τ and σ_u shown in the panels, where $u = 1/R$. As the distributions are symmetric about their peaks, and these parameters are uncorrelated with one another, we take the fluctuations to be random. These small relative fluctuations can be considered as independently affecting the pulse collapse location z_{cl}, whose standard deviation can then be written as $\sigma_{z_{cl}} = [\sigma_\varepsilon^2(\partial z_{cl}/\partial\varepsilon)^2 + \sigma_\tau^2(\partial z_{cl}/\partial\tau)^2 + \sigma_u^2(\partial z_{cl}/\partial u)^2]^{1/2}$, with the gradient $(\partial/\partial\varepsilon\,, \partial/\partial\tau\,, \partial/\partial u)z_{cl}$ determined from many shots measuring z_{cl} vs. (ε, τ, u) and evaluated at the mean point $(\bar{\varepsilon}, \bar{\tau}, \bar{u})$. The expression for $\sigma_{z_{cl}}$ can be used to isolate the contributions of each of the fluctuating variables on the pulse collapse location. To do this, the nominal pulse energy or pulse duration are fixed while the other parameter is scanned beyond the standard deviations (σ_ε or σ_τ) to determine the value of the partial derivatives more accurately than from the points clustered within the standard deviations. For the wavefront curvature, independent control of u was experimentally difficult; however σ_u was sufficiently wide to provide a reasonable value for $\partial z_{cl}/\partial u$.

The results of these scans are shown in Fig. 2.3, where the green lines are a second order polynomial least squares fit whose local slope, through $\bar{\varepsilon}, \bar{\tau},$ and $\bar{u}$, is shown in the panels. The vertical spread in z_{cl} points, for example in Fig. 2.3(a) for a

fixed value of ε, reflects the fluctuations in τ and u. Similarly, the spreads in z_{cl} in Fig. 2.3(b) and in Fig. 2.3(c) reflect the fluctuations in (ε, u) and (ε, τ), respectively. Importantly, the vertical spread appears roughly constant within each of the panels of Fig. 2.3. This further reflects the lack of correlation among the parameters.

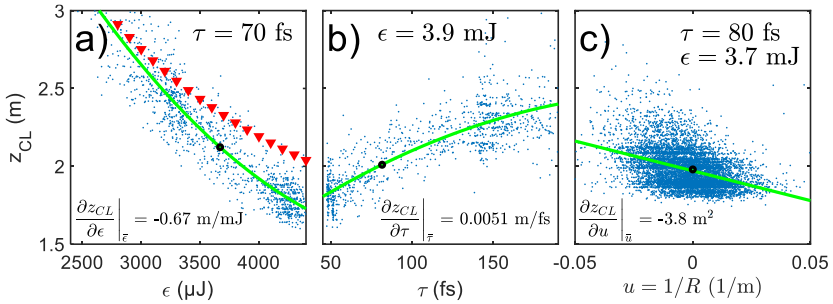

Figure 2.3 (a) Collapse location (from down-collimating telescope) vs. scanned pulse energy and **(b)** pulse duration. **(c)** Collapse location vs. intrinsic fluctuations in wavefront curvature. Green curves: quadratic best fits to data points. The black circles indicate the values $\bar{\varepsilon}, \bar{\tau}, and\ \bar{u}$. The red triangles in (a) are from an UPPE simulation without turbulence.

For the collimated beam of Fig. 2.2(a) and 2.2(b), using $\sigma_\varepsilon = 98\ \mu J$ and $(\partial z_{cl}/\partial \varepsilon)_{\bar{\varepsilon}} = -0.67$ m/mJ from Fig. 2.3(a), we expect that pulse energy fluctuations alone would give a standard deviation of collapse location $\sigma^{\varepsilon}_{z_{cl}} \sim \sigma_\varepsilon |(\partial z_{cl}/\partial \varepsilon)_{\bar{\varepsilon}}| \sim 6.6$ cm. Similarly, for pulse width variations alone, $\sigma^{\tau}_{z_{cl}} \sim \sigma_\tau |(\partial z_{cl}/\partial \tau)_{\bar{\tau}}| \sim 1.5$ cm and for intrinsic phase front fluctuations, $\sigma^{u}_{z_{cl}} \sim \sigma_u |(\partial z_{cl}/\partial u)_{\bar{u}}| \sim 5.7$ cm. Therefore, energy and phase front fluctuations are much more important than fluctuations in the pulse duration for determining the repeatability of filaments. It is evident that air turbulence, even in a lab, is an important factor over distances of even a few meters.

We modeled the experiment of Fig. 2.2 using a 2D+1 (2D space plus time) GPU-based simulation using the unidirectional pulse propagation equation (UPPE) [66,67], which includes the Kerr and molecular rotational response of air, plus ionization. To model the effect of energy variations alone, these simulations do not

include turbulence. The resulting simulation points (red triangles) are overlaid in Fig. 2.3(a), showing good agreement with the measurements, especially at lower pulse energy. To simulate turbulence (see later), we used a modified von Karman spectrum with a 1 mm inner scale and 1 m outer scale [53], seeded it with random noise, and inverse Fourier transformed it to generate 2D phase screens [68] every centimeter.

To determine the wavefront fluctuations from beam propagation *before* the spatial filter, where the beam was enclosed by a sealed box inside a tent with a HEPA (High-efficiency particulate air) filter, the wavefront sensor was placed immediately following the filter. Based on a 10,000 shot sample, we measured $\sigma_{z_{cl}}^{u} = 0.0042\ \mathrm{m}^{-1}$, which we attribute mainly to fluctuations in thermal lensing in the laser rods. This spread is more than 3× smaller than $\sigma_{z_{cl}}^{u} \sim 0.015\ \mathrm{m}^{-1}$ at the down-collimator.

Further exploring the effects of turbulence on femtosecond pulse collapse, we employed the turbulence box preceding the reflective telescope, as shown in Fig. 2.1. For this experiment, the laser parameters were $\varepsilon = 2.8$–2.9 mJ and $\tau = 45$ fs. Here, since stronger turbulence was localized to a short axial region, its strength was determined using $C_n^2 L = \theta^2 D^{1/3}/2.91$ [69], which depends on the angular deflection θ (rad) of the λ = 532 nm probe beam, the average beam diameter D, and the length L (= 15 cm) of the turbulence box. Fig. 2.4(a) plots C_n^2 versus heater voltage, while Fig. 2.4(b) plots $\sigma_{z_{cl}}$ and mean collapse location $\overline{z_{cl}}$ versus $C_n^2 L$. For each heater tape voltage in this experiment, several (3-5) 1000 frame (each 1 ms) sets were taken to determine $C_n^2 L$, and seven sets of 1000 filament shots were taken. These sets were taken to cover potential laser and environmental drifts during our

runs. As seen in Fig. 2.4(a), over the voltage scan 10-100 V, $C_n^2 L$ ranged from 2.7×10^{-13} m$^{1/3}$ to 1×10^{-11}m$^{1/3}$. Fig 2.4(b) plots the standard deviation of the collapse location and the mean collapse location, where it is seen that $\sigma_{z_{cl}}$ increases with $C_n^2 L$ but $\overline{z_{cl}}$ is roughly constant. Histograms of z_{cl} are plotted in Fig. 2.4(c), showing the increased spread in collapse location for increased heater voltage and turbulence. We modeled the collapse variability for 60 V with a run of 50 3D+1 UPPE simulations including room turbulence ($C_n^2 L \sim 6.4 \times 10^{-13}$ m$^{1/3}$ for the $L \sim 10$ m propagation path from the spatial filter to the telescope) and the turbulence box ($C_n^2 L \sim 2.4 \times 10^{-12}$ m$^{1/3}$ over 15 cm), giving $\sigma_{z_{cl}}^{sim} = 19$ cm, agreeing with $\sigma_{z_{cl}} = 21.5$ cm at 60 V in Fig. 2.4(c).

We note that the propagation simulations in [38,70] predict a reduction in $\overline{z_{cl}}$

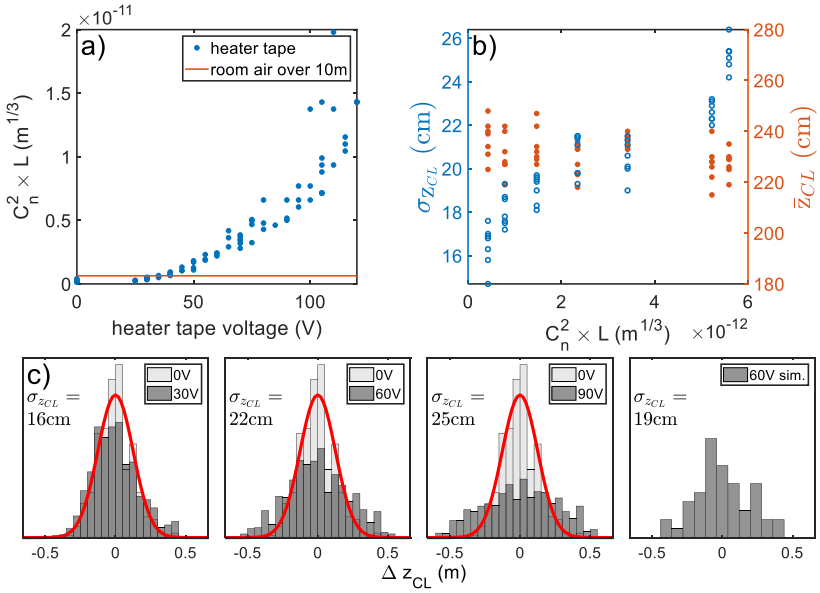

Figure 2.4. (a) $C_n^2 L$ measured in turbulence box (using a λ = 532 nm probe) vs. heater tape voltage. The brown baseline is the room turbulence level. **(b)** Mean collapse location $\overline{z_{cl}}$ and standard deviation $\sigma_{z_{cl}}$ vs. turbulence strength. **(c)** Histograms of collapse location Δz_{cl} relative to $\overline{z_{cl}}$ vs. heater tape voltage. The histogram for each voltage overlays the V = 0 histogram, whose best-fit Gaussian is the red curve. Right panel: Histogram for 50 3D+1 UPPE simulations for 60 V.

with increased turbulence, in contrast to our experiments and simulations. However, the beams simulated in [38] are larger than the turbulence inner scale of ~1 mm, and are more susceptible to turbulent variations than our $w_0 \sim 1.7$ mm beams.

2.4 Summary

To summarize, we have performed measurements recording the full axial energy deposition profile of a nonlinearly propagating laser pulse over macroscopic laboratory distances in a single shot, using a linear array of synchronized microphones. In particular, we have examined the sensitivity of pulse collapse of high peak power femtosecond pulses to fluctuations in pulse width, pulse energy, and wavefront curvature. We have found that pulse energy and room air turbulence-induced wavefront curvature fluctuations are the dominant contributions. The important role of air turbulence, even over relatively short distances in the laboratory, is confirmed through 3D + 1 propagation simulations.

Chapter 3: Dynamics of femtosecond laser-triggered spark gaps

3.1 Introduction

In the previous Chapter we presented single shot measurements of axially resolved filament energy deposition over distances up to one meter. Energy deposition over these distances is useful for generating air waveguides as will be discussed in Chapter 4 but suffers from collapse location instability due to air turbulence. Lens assisted filamentation overcomes collapse location instability but generally produces shorter filaments. In this chapter we will focus on an application of filament energy deposition over ~10 cm and in the process investigate the evolution of a filament plasma and post-filament density hole in the presence of strong DC electric fields. We present space and time resolved measurements of the air hydrodynamics induced by femtosecond laser pulse excitation of the air gap between two electrodes at high potential difference. We explore both plasma-based and plasma-free gap excitation. The former uses the plasma left in the wake of femtosecond filamentation, while the latter exploits air heating by multiple-pulse resonant excitation of quantum molecular wavepackets. We find that the cumulative *electrode-driven* air density depression channel plays the dominant role in the gap evolution leading to breakdown. Femtosecond laser heating serves mainly to initiate the depression channel; the presence of filament plasma only augments the early heating.

3.2 Laser triggered spark gap

Considerable work has been done over the past several decades investigating the triggering of high voltage (HV) gas discharges by intense laser pulses. Spark gap discharges are used in widespread applications including HV surge protection and power switching, high energy laser triggering, and as ignition sources in combustion engines. The theory of spark-gap discharges is rich in basic physics and has been discussed at length in the literature [71–80]. Spark gaps rely on acceleration of free electrons between the cathode and anode by the gap electric field, driving further ionization by collisional avalanche ionization. In the conventional picture, breakdown starts with the development of one or more 'streamers', i.e. avalanche-ionization induced protrusions of charge, which under the action of additional resistive heating of the gas and consequent lowering of neutral gas density, create a higher conductance channel bridging the cathode and anode. Laser heating of the intra-gap gas can enable control of the discharge current path [81]. The use of low energy ultrafast laser pulses can improve this control by generating, via multiphoton or field ionization, a continuous extended length of low density plasma [82]. Extended focal volumes can be generated by optical elements such as cylindrical lenses or axicons [82] or by relying on nonlinear self-guiding by femtosecond filamentation [8,83]. In the case of filamentation in air, on-axis electron densities are typically $\lesssim 10^{16}$ cm^{-3} [33], constituting only ~0.1% fractional ionization at atmospheric density. Few-nanosecond Q-switched lasers, by contrast, can generate higher plasma densities through electron avalanche, but longitudinally extended and contiguous energy deposition is a challenge. The use of double pulse schemes [82,84] or picosecond

lasers [46] have been proposed as solutions providing higher density contiguous plasmas.

Regardless of the pulsewidth used, laser triggering of HV discharges in past work has depended on gas ionization by the laser, with the discharge initiated either by the newly conductive channel enabled by the plasma [85], or by the reduced gas density channel driven hydrodynamically by the gas heating [86–88], where in the latter case the lower density reduces the breakdown threshold electric field [89]. For femtosecond pulses, because of the relatively low plasma densities and conductivity generated, it has been proposed that hydrodynamic response and on-axis density reduction is the primary mechanism responsible for discharge initiation [87,88]. Femtosecond filament triggered HV discharges have been widely studied in recent years, with applications envisioned to include reconfigurable RF antennas and guiding of electrical pulsed power, including lightning [60,90–94].

Early work by Loeb [76–78] and Meek [79] explained HV breakdown discharges in terms of streamer formation. The role of streamers and the associated phenomena of leaders and corona discharge have generated much discussion in the femtosecond laser discharge literature on both long and short spark gaps in air. Several groups have determined that corona generation and leader formation are important for filament-guided HV breakdowns in air [87,95–97]. Gordon et al. demonstrated a mode of discharge which can proceed without the aid of streamers, where electric field-driven resistive heating by free electrons in the gap increases the temperature and plasma lifetime, leading to breakdown [98]. Schmitt-Sody et al. also demonstrated streamer-free HV discharges triggered by > 2ps duration pulses [99].

In this Chapter we perform space- and time-resolved measurements of the plasma and gas evolution in a high voltage electrode gap at times after the application of an ultrashort laser pulse or pulse train up to the time of breakdown. We find that the cumulative electrode-driven air density depression channel initiated by the laser and sustained by the gap field plays the dominant role in the gas evolution leading to breakdown. Even at voltages well below breakdown, the cumulative resistive heating induced by the gap field acts to deepen and widen a reduced density air channel between the electrodes. Approaching breakdown, the air channel guides the streamers, promotes secondary ionization, and reduces the threshold voltage. We show that the size of the initial axial air density depression induced by the laser, irrespective of whether plasma is initially present or not, is what is most important for initiating a discharge. Below the breakdown threshold, we find that the transient currents induced by femtosecond laser excitation of the gap decay on a timescale consistent with transverse thermal diffusion of the reduced density channel.

3.3 Experiment

The spark gap consists of two hemispherical tungsten electrodes of radius $a_{elec} = 1.27$ cm spaced 3–10 mm apart, with 2 mm diameter axial holes for entrance and exit of the heating laser pulse or pulse train, plus an interferometric probe pulse (see Fig. 3.1(a)). To generate pulse trains, single pulses from a Ti:Sapphire laser (λ = 800 nm) were first passed through a nested interferometer [100] ('pulse stacker') which generates eight replica pulses, with the inter-pulse delays controlled by motorized translation stages (~10 fs step size). For single pulse experiments, all but

one of the pulse stacker arms was blocked. The pulse or pulse train was then passed through an adjustable grating compressor allowing control of the pulsewidth. Inserting the pulse stacker upstream of the compressor avoided nonlinear distortion in the stacker's beamsplitting optics. The laser was then axially focused through the electrode holes (using a $f = 50$ cm lens at $f/45$), giving a confocal parameter of $2z_0 = 4$ mm and $1/e^2$ intensity radius $w_0 = 23$ μm, with the beam waist placed midway between the electrodes. In general, the axial extent of the gas excitation was longer than $2z_0$ owing to the onset of self-focusing and filamentation, as discussed later.

As shown in Fig. 3.1(a), the electrodes were connected in parallel with a C = 4.4 nF capacitor bank, which was charged through a 1 kΩ resistor up to +30 kV by a DC HV power supply (Spellman High-Voltage model SL30PN10). The diode, inductor, and capacitor near the power supply act as an RF choke to shunt to ground any strong transients from the spark gap breakdown. A current measurement circuit (inside the green dashed box) is inserted in series with the spark gap ground electrode for some of our measurements. Fig. 3.1(b) shows numerical solutions of Laplace's equation giving the on-axis electric field $E_z(z)$ between the electrodes for a range of electrode spacings and a nominal gap voltage of 10 kV. The two short vertical black lines on each curve indicate the front faces of the two hemispherical electrodes, with the electric field quickly decreasing inside the electrode central holes. For electrode gaps $\gtrsim 4$ mm, $E_z(z)$ is reasonably uniform between the electrodes. The gas and plasma evolution between the electrodes was monitored by a variably delayed interferometric probe pulse (λ = 532 nm, 10 ns) electronically synchronized (~1 ns

jitter) and co-propagating with the femtosecond air excitation pulse(s) (see Fig. 3.1(a)). The probe pulsewidth and timing jitter were small compared to the onset timescale of breakdown (see below).

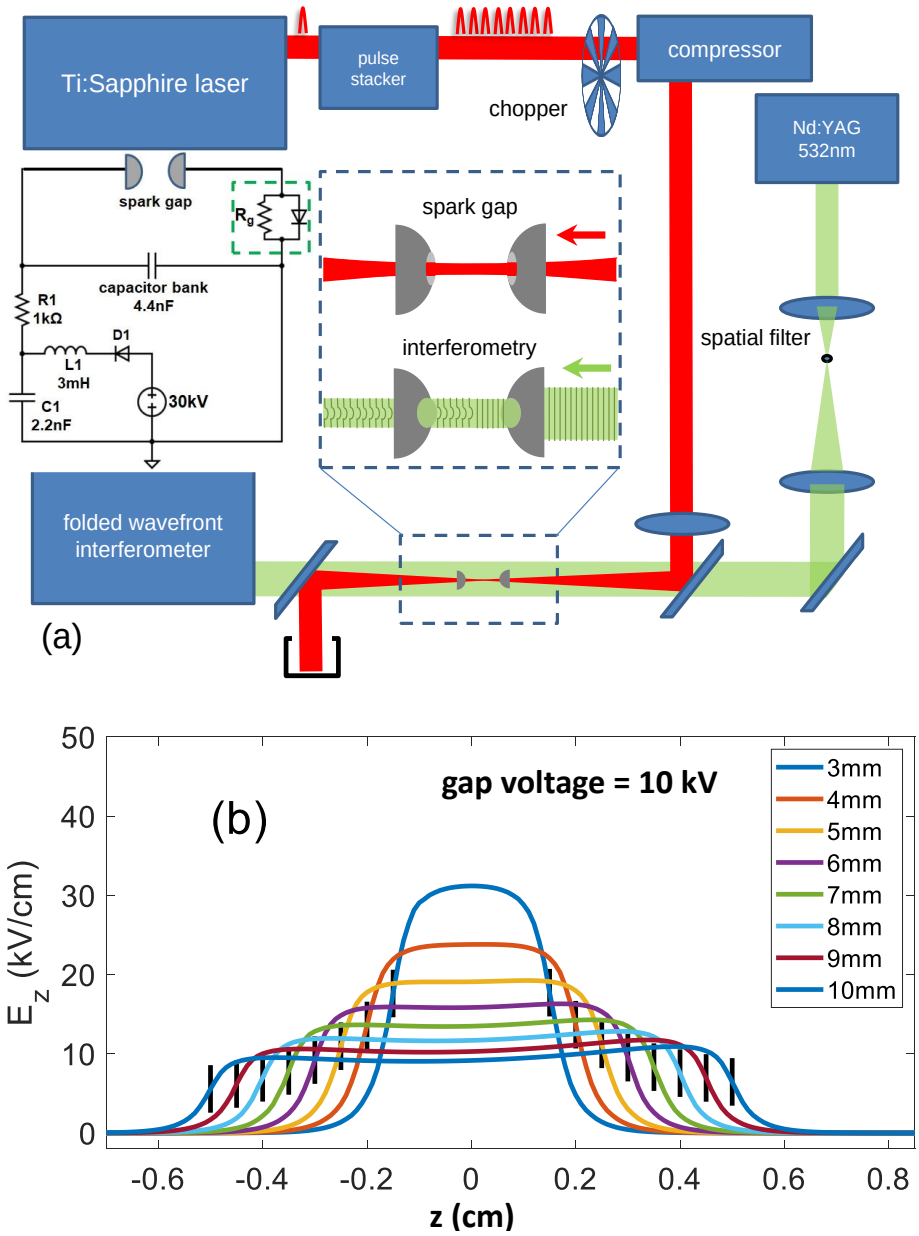

Figure 3.1 (a) Optical setup for investigating gas density dynamics initiated by a λ=800 nm femtosecond laser pulse or pulses in a high voltage spark gap. The magnified view shows the femtosecond excitation pulse and λ=532 nm, 10 ns probe pulse propagating axially through the spark gap electrodes. Arrows depict the direction of propagation. Also shown is the spark generation circuit, with the green box depicting an auxiliary current monitor. **(b)** Simulated on-axis axial field E_z for a range of electrode separations for 10 kV gap voltage. Fields for different gap voltages are obtained by linear scaling. The two vertical black bars on each curve indicate the front faces of the hemispherical electrodes.

The interaction region was end-imaged through the hole in the positive electrode onto a folded wavefront interferometer, with the object plane adjustable. Interferometric background images (femtosecond pulse off) were taken on every shot by passing the pulse(s) through an optical chopper before the compressor. The probe beam was cleaned by a spatial filter prior to the interaction region, producing smooth, low noise phase fronts. With use of the chopper, our single shot interferometric measurements were limited to a noise floor of < 40 mrad. Extraction of interferometric phase $\Delta\varphi(\mathbf{r}_\perp)$ was performed as in ref. [50], yielding refractive index perturbation profiles $\Delta n(\mathbf{r}_\perp)$ axially averaged over the gap width, where $\mathbf{r}_\perp$ is a transverse coordinate with respect to the spark gap axis.

3.4 Results

Fig. 3.2 shows a time sequence of air density perturbation profiles $\Delta N(\mathbf{r}_\perp)/N_0 = \Delta n(\mathbf{r}_\perp)/(n_0 - 1)$ following application of a 65 μJ, 100 fs FWHM laser pulse to a 5.5 mm electrode gap for (a) 0V and (b) 17 kV/cm applied to the gap. Here N_0 and n_0 are the background air density and refractive index, respectively. Based on measurements and simulations in our prior work [3,6,50], the profiles in (a) are explained as follows. When a 50-100 fs laser pulse is focused into air, energy is deposited primarily through optical field ionization and non-resonant rotational Raman excitation of the air molecules (the laser bandwidth is not wide enough for vibrational Raman excitation) [44].

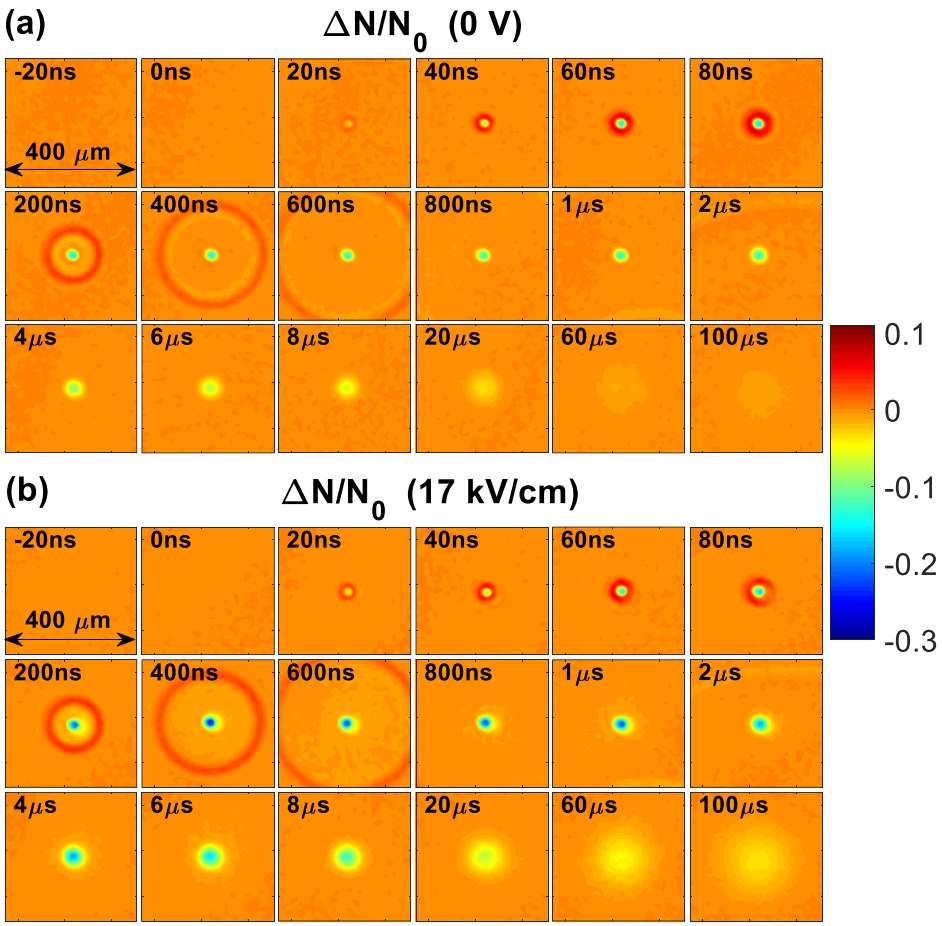

Figure 3.2 (a) Evolution of refractive index shift profiles $\Delta n(\boldsymbol{r}_\perp)$ at a sequence of probe delays following heating at $t = 0$ by a single 100 fs, 65 μJ laser pulse in the spark gap with zero gap field. The outward propagating orange ring, seen in the frames at delays < 800 ns, is a single-cycle acoustic wave. **(b)** Same measurement as (a), but with 17 kV/cm gap field. In the case of HV applied across the gap, the on-axis density hole is observed to deepen and widen relative to the 0 V case at all delays, and acoustic wave amplitude is larger. Gap length=5.5 mm.

The laser-produced plasma recombines to neutral gas on a <10 ns timescale [33,63], while the excited molecular rotational wavepacket collisionally decoheres on a ~100 ps timescale [44]. Owing to the finite thermal conductivity of the surrounding air, the deposited laser energy remains contained in a narrow radial zone, but is repartitioned into the translational and rotational degrees of freedom of the neutral gas [50]. For femtosecond filamentation in atmosphere, the radial zone has approximately the filament core radius of a_{core}~50 μm [33,50,101]. The result is an extended region of high pressure at temperatures up to a few hundred K above

ambient [6]. The onset of this pressure spike is much faster than the acoustic timescale of the gas, $a_{core}/c_s \sim 100$ ns, where $c_s \sim 3.4 \times 10^4$ cm/s is the air sound speed, so that it impulsively launches a cylindrical single-cycle acoustic wave ~100 ns after the filament is formed [3], as seen in Fig. 3.2(a). Later panels show that by ~1 μs, the acoustic wave has long since left the filament region, leaving a density depression ('density hole') at elevated temperature and in pressure equilibrium with the surrounding gas. Over $> \sim 1$ μs to ~1 ms, the density hole decays by thermal diffusion, becoming shallower and wider.

After pressure equilibrium has been achieved, the 'area' of the density hole profile is a proxy for the laser energy deposited per unit length in the gas, as shown in ref. [1],

$$\varepsilon_{abs} = -(k(n-1))^{-1} c_v T_0 \rho_0 \int \Delta\varphi(\mathbf{r}_\perp)\, d^2\mathbf{r}_\perp \qquad (3.1)$$

where c_v is the specific heat of air at constant volume, ρ_0 and T_0 are the ambient gas density and temperature, $k = 2\pi/\lambda$ is the probe wavenumber, and n is the gas refractive index. While Eq. (3.1) was applied in ref. [1] to femtosecond laser-generated density holes, it will also apply to calculating energy deposited by any heating mechanism that is fast compared to thermal diffusion into the surrounding gas, which has a ~millisecond timescale. We use this broader applicability of Eq. (3.1) in much of the analysis of this paper.

3.4.1 Effect of filament density hole and plasma on high voltage breakdown

We first assess the roles of the laser produced plasma and the gas density depression in the high voltage breakdown process. A first set of experiments was performed in which air density holes of the same depth were generated, either with or without initial plasma. In the case of a single filamenting pulse that generates plasma in the usual manner, the pulse energy was chosen (22 μJ, 100 fs) to produce an on-axis density hole depth $\Delta N/N_0 \sim 3\%$ at 1 μs delay after the pulse, where N_0 is the background air density and ΔN is the on-axis density reduction. In the plasma-free case, we achieved the same $\Delta N/N_0 \sim 3\%$ hole depth at 1 μs delay by using an 8-pulse sequence of 12.5 μJ, 100 fs pulses (below the ionization threshold of the oxygen molecule) from the pulse stacker to rotationally heat the air's nitrogen molecules. The inter-pulse timing in the sequence was adjusted to ~ 8.3 ps (the rotational revival time of N_2) in order to maximize the rotational wavepacket excitation and air heating [5]. On the basis of oxygen's ionization rate intensity dependence, $\propto I^8$, we expect single pulse excitation to produce at least $(22\ \mu J/12.5\ \mu J)^8 \sim 90\times$ more plasma than the pulse sequence.

Fig. 3.3(a) shows, for the plasma and near plasma-free cases, the energy deposited in the gas between the electrodes (calculated using Eq. (3.1) from the gas density hole measured at 1 μs probe delay) as a function of applied gap field. The gap field used here and in all other figures is the average electric field $\langle E_z \rangle$ between the electrodes calculated from Fig. 3.1(b). Each point is an average over 25 consecutive laser shots, while the error bars correspond to the standard deviation. The plotted points terminate where breakdown occurs. Below ~13 kV/cm, the energy absorbed in the gas (~0.05 μJ) in both cases is consistent with the $\Delta N/N_0 \sim 3\%$ density hole

imprinted by the single pulse or pulse train. Above ~13 kV/cm, there is increasing gas heating in the single pulse (plasma) case, consistent with electron impact ionization and resistive heating driven by the high voltage. At the ~13 kV/cm threshold, $eE_{gap}\lambda_{mfp}$~1 eV for a mean free path in air $\lambda_{mfp} \sim 0.5$ μm [102,103]. This is sufficient for electrons to reach several eV over multiple collisions or in the tail of the distribution, enough energy to surmount the nitrogen vibrational $^2\Pi_g$ shape resonance peaking past ~2 eV [102]. We speculate that because of this vibrational energy sink, gap fields below ~13 kV/cm are unable to accelerate electrons sufficiently to accumulate the ~12-15 eV needed for impact ionization of O_2 and N_2.

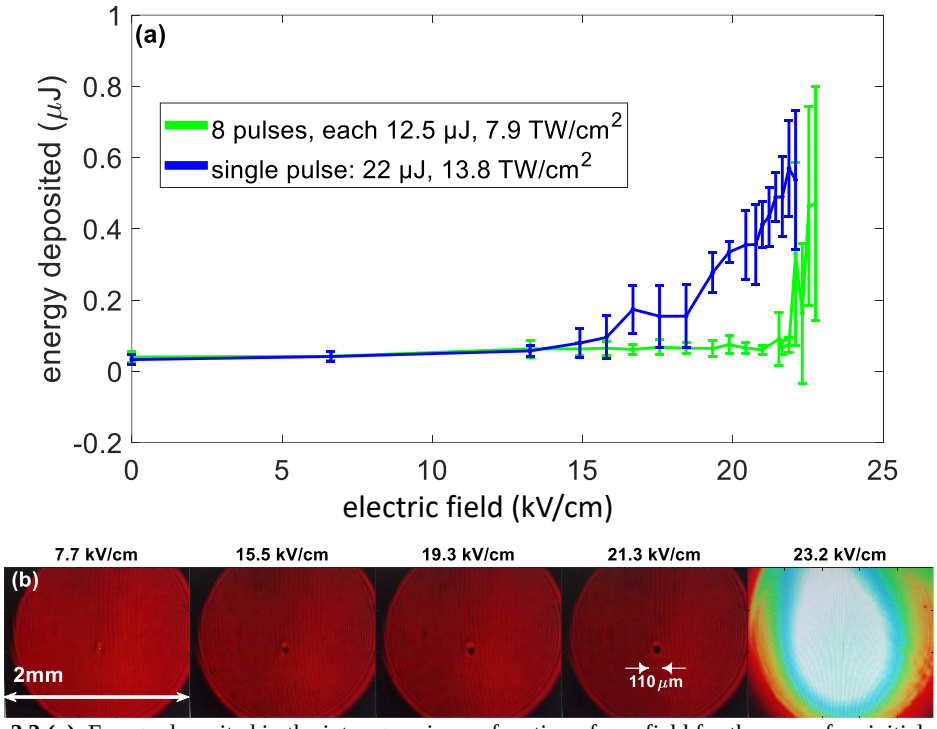

Figure 3.3 (a) Energy deposited in the intra-gap air as a function of gap field for the case of an initial plasma (blue curve, single 22 μJ laser pulse) and the case of negligible plasma (green curve, 8 pulse sequence with 12.5μJ/pulse). The electrode spacing is 4 mm. For the blue curve, a single laser pulse formed a plasma filament between the electrodes. For the green curve, the air in the electrode gap was heated via N_2 rotational excitation by the resonant 8-pulse sequence. In both cases, the initial on-axis density hole depth was $\Delta N/N_0$ ~3% at a delay of 1μs. **(b)** End-view shadowgrams (through positive electrode) of the gas density hole initiated by single 22 μJ pulse and subsequently deepened/widened by increasing gap fields. The circular edge in the red images is the electrode central hole edge. Probe delay = 3μs. The 23.2 kV/cm frame shows an end view of the breakdown flash. The breakdown is centered on the density hole.

Both the additional carriers and the higher energy electrons then heat the air via elastic and inelastic collisions, rapidly deepening the density hole and increasing λ_{mfp} until the onset of breakdown at ~22 kV/cm, as seen in the blue curve. In both plasma-free and plasma cases, however, the breakdown threshold is ~22-23 kV/cm, and occurs roughly where the energy absorbed by the gas (as measured by the density hole area (or volume = area×length)) is comparable at ~0.5μJ. This suggests that the density hole is the main factor in setting the breakdown threshold. To the extent that pre-existing free electrons are involved, their acceleration in the gap field serves mainly to heat the air to augment the density hole. In the nominally plasma-free case (green curve), pre-breakdown gas heating has occurred, but mainly at fields just below the breakdown level. In another view of the dynamics induced by a single pulse, Fig. 3.3(b) shows the deepening and widening of the density hole with increasing gap field, until breakdown, centered on the density hole, occurs at ~23 kV/cm.

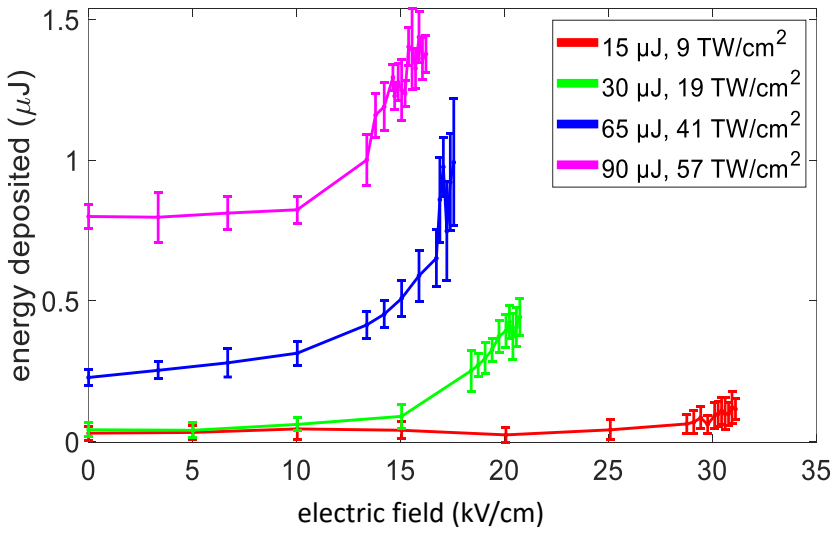

Figure 3.4 Energy deposited in the intra-gap air as a function of the input laser pulse energy and gap field for a 5.5 mm gap. The curves terminate at the point of breakdown.

In the next set of experiments, we examined the effect of the energy of a single filamenting (plasma-producing) laser pulse on the onset of breakdown. Fig. 3.4 plots energy deposition, determined via Eq. (3.1), as a function of gap field (gap length 5.5 mm) for four laser pulse energies. It is seen that for higher pulse energy, more energy is deposited in the gap and the gap breakdown field (where the curves terminate) is reduced. At fields below the sharp upturn of each curve, the energy deposition is seen to slowly increase or stay roughly constant. For each curve, the upturn is associated, as in Fig. 3.3, with the onset of sufficient electron acceleration for impact ionization of O_2 and N_2 along with increasing gas heating and widening/deepening of the density hole, which increases channel conductivity. The higher initial electron densities generated by higher laser energies establish larger density hole volumes, leading to onset of breakdown at lower gap fields.

3.4.2 Electrode separation

Fig. 3.5(a) demonstrates the dependence of air heating in the gap (by a single 75 μJ pulse) as a function of gap electric field for a range of electrode separations (4-10 mm). Each curve in Fig. 3.5(a) terminates at the breakdown field near ~15 kV/cm. For the smaller gaps, the effective breakdown field is slightly larger (~16 kV/cm) because, as seen in Fig. 3.1(b), the field peaks over a smaller fraction of the gap width. For the longer gaps, the peak field occupies a larger fraction of the gap; the breakdown field converges to ~14-15 kV/cm.

In all of these runs, the laser vacuum confocal parameter is $2z_0$ ~ 4 mm centered on the gap, with spot size $w_0 = 23\ \mu m$. However, filamentary propagation

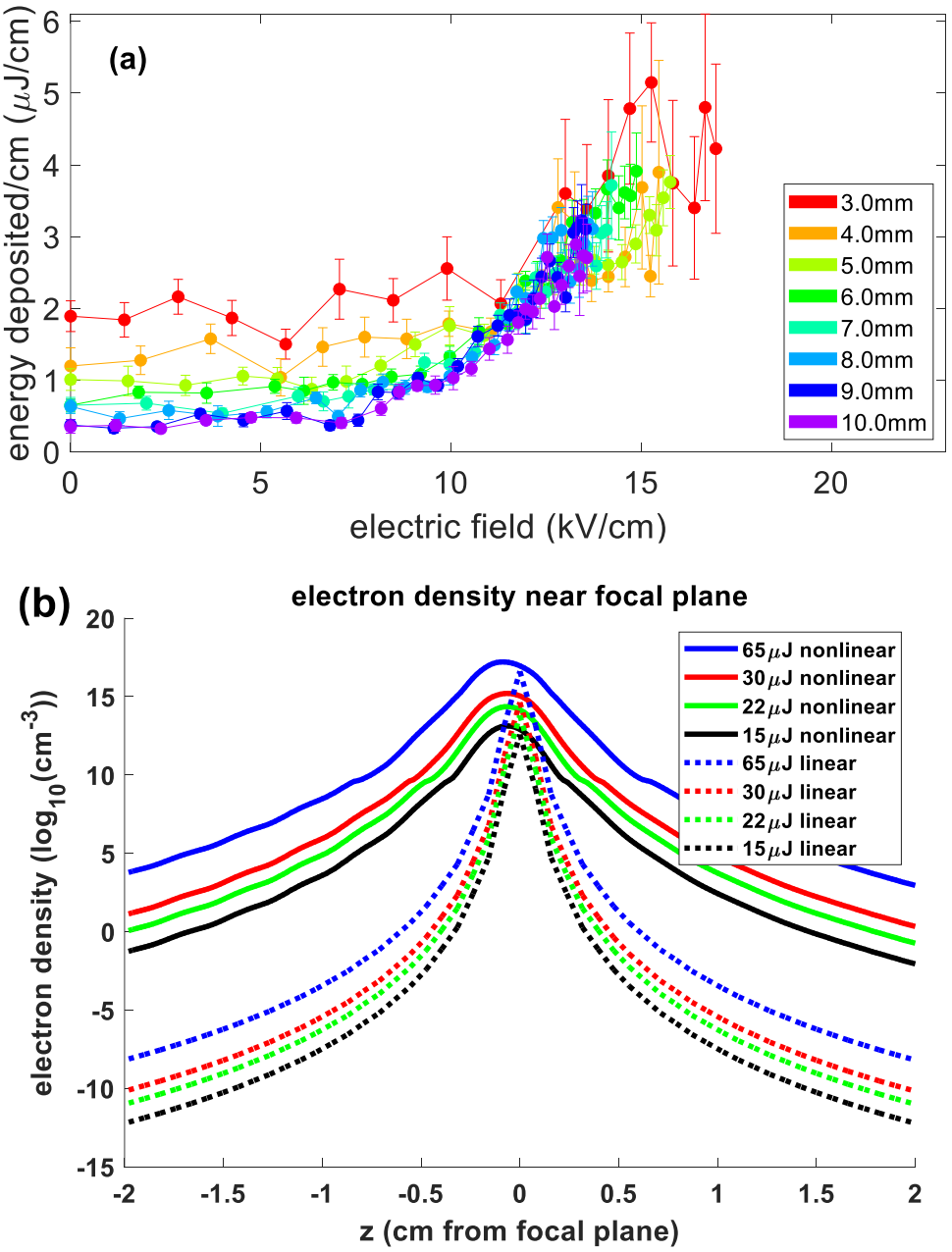

Figure 3.5 (a) Energy deposited per unit length after single 75 μJ laser pulse excitation for a range of gap fields and gap separations. **(b)** Propagation simulation showing the plasma-extending effect of filamentation. The laser propagates left to right. By comparison, the multiphoton ionization yield of a linearly propagating pulse is many orders of magnitude lower away from the linear beam waist. It is seen that filament peak electron density occurs slightly upstream of the linear beam waist consistent with self-focusing and filamentation.

is responsible for extended plasma generation, increasing the electron density away from the vacuum beam waist by many orders of magnitude. This is seen in the filamentation simulations of Fig. 3.5(b), which are compared to the $\propto (I(z))^8$

ionization yield of a linearly propagating pulse. These simulations were performed with a GPU implementation of the unidirectional pulse propagation equation, which includes the full molecular response of air [66,67]. The plots of Fig. 3.5(a) show that for low fields, the energy deposition per unit length remains roughly constant, and is higher for smaller gaps. This is consistent with laser energy deposition from the filament plasma, whose axial average electron density is higher for short gaps (see Fig. 3.5(b)). Only once the field increases to ~8 kV/cm, the curves for all gaps begin to converge as resistive heating (by electrons driven by the gap field) begins to dominate.

3.4.3 Temporal evolution of gas heating

Without applied HV, after the filament-heated air sheds its single cycle acoustic emission and achieves pressure equilibrium (as seen in Fig. 3.2(a) for $t > \sim 200$ ns), the density hole decreases in depth and widens as thermal diffusion occurs to the surrounding air. With the application of HV across the gap, the gas is heated for at least ~100μs (see below) after the initial filament energy deposition (as seen by the HV-driven widening and deepening of the density hole in Fig. 3.2(b)). Fig. 3.6 shows plots of the gas heating as a function of time in a 5.5mm gap for a range of voltages for a fixed filamenting laser pulse (65 μJ, 100 fs). The highest voltage was intentionally kept just below the breakdown threshold. By $t = 200$ ns (indicated by the vertical black line), the acoustic wave has just been shed from the density hole. It is only after that time that Eq. (3.1) can be used to determine absorbed energy. It is seen that by ~200 ns, the gap HV has already heated the air, as indicated by the

increasing density hole volume with gap voltage, and heating is shown increasing out to at least ~100 μs. This heating remains predominantly localized to the density hole region imprinted by the initial laser pulse, as seen in Fig. 3.2(b) and Fig. 3.3(b).

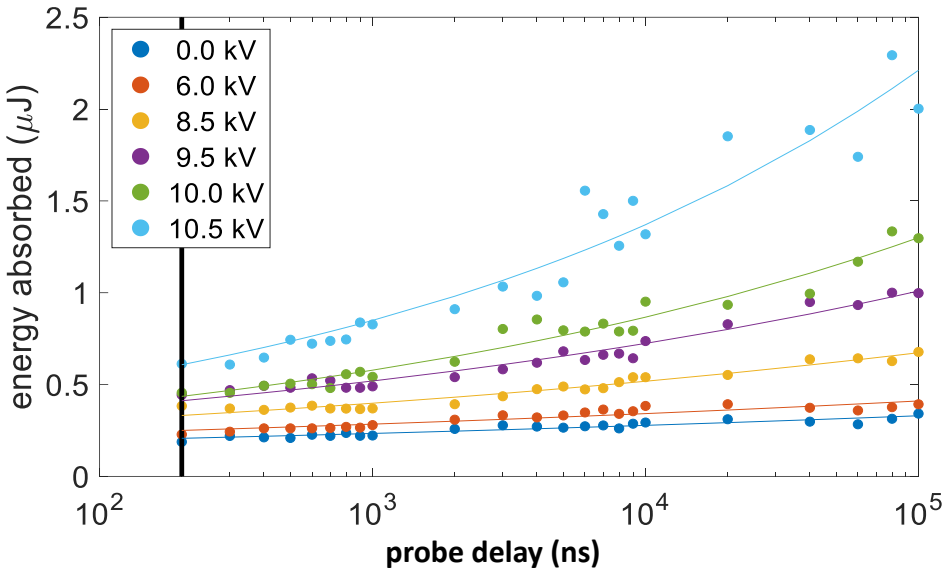

Figure 3.6 Energy absorbed by intra-gap air vs. probe delay for several gap voltages. Single 65 μJ, 100 fs laser pulse, 5.5 mm gap. The vertical bar corresponds to $t = 200$ ns probe delay, after which Eq. (1) can be applied. The density hole volume (=area×length) is seen to continuously increase out to the maximum probe delay of 100 μs, with an increasingly rapid increase with gap voltage. Each point is an average of 25 shots, and the curves are best fits of the points to $y = at^b$. Even by 200ns, higher gap voltages drive significant heating.

3.4.4 Pre-breakdown current

To help understand the origin of the pre-breakdown air heating, we inserted an auxiliary current monitor shown by the dashed green box in Fig. 3.1(a). It consists of a resistance $R_g = 9.1$ MΩ in parallel with a miniature gas discharge tube (LittelFuse CG110) linked to ground from the gap electrode. The discharge tube acts as a shunt to ground for the extremely large transient currents generated at spark gap breakdown. A high voltage probe (Tektronix P6139B) measures the time-resolved voltage $V_R(t)$

and gap current $I_{gap}(t) = V_R(t)/R_g$ for gap voltage below the breakdown threshold, where R_g includes the contribution of the voltage probe resistance.

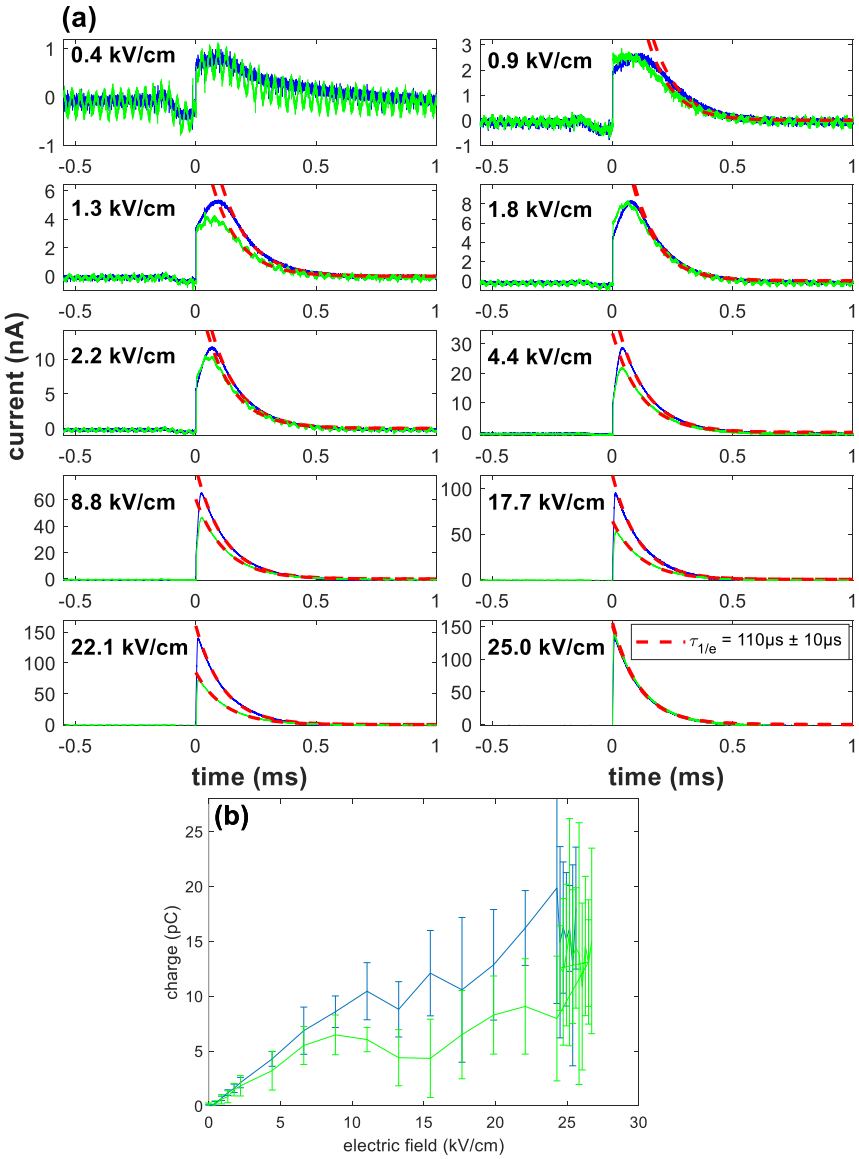

Figure 3.7 (a) Gap current initiated by single 22μJ, 100 fs laser pulse (blue curves, initial plasma present) or 8-pulse 12.5 μJ, 100fs sequence (green curves, negligible initial plasma) vs. gap field in a 4mm gap. Dashed red lines are exponential fits to the curve decay portions; all fits have $\tau_{1/e} = 110 \pm 10\ \mu s$, as indicated in bottom right panel. Curves are 10 shot averages. **(b)** Pre-breakdown charge driven across gap vs. gap voltage. The curves terminate at breakdown.

Results are shown in Fig. 3.7(a) for both the single 22 μJ, 100 fs filamenting laser pulse (blue curves) and the 8-pulse (12.5 μJ, 100 fs) resonant sequence (green curves) in a 4 mm gap for gap fields below breakdown. Recall that the single pulse

and pulse sequence generate a similar initial air density depression, but the single pulse generates plasma while there is negligible plasma from the pulse sequence. In both cases, the gap current exhibits a sharp rise at $t = 0$ immediately after application of the laser pulse, followed by a rollover and then a decay, which is well-fitted by exponentials (dashed red lines) with $\tau_{1/e} = 110 \pm 10$ μs applying to all curves. The measured sharp rise onset of ~10 ns is limited by the probe and oscilloscope frequency response. As the gap field increases, the rollover part of the curves shorten. For lower gap fields we see that the rollover duration is $< \sim 0.25$ ms, much longer than the <10 ns timescale for filament plasma recombination. This, plus the fact that the blue curves (initial plasma present) and green curves (negligible initial plasma) are similar, suggests that the driven currents are electrode-supplied; the filament-generated free electrons play a negligible direct role in the blue curves—their main, indirect, role is to initially heat the air to generate a density depression channel. This is also seen in the absorbed energy measurements at early times in Fig. 3.6.

We attribute the fast initial rise of the current in Fig. 3.7(a) to rapid streamer onset and preferential channeling through the initial axial density depression. The heating effect from preferential channeling of gap current is directly seen by comparing Fig. 3.2(b) to Fig. 3.2(a). The slow initial current increase during the rollover accompanies increasing resistive heating and channel deepening. When transverse thermal diffusion has widened the channel sufficiently, as seen in Fig. 3.2, the local current density drops and resistive heating decreases—the accompanying increase in gap resistance leads to a slow decrease in the current as the air gap returns to equilibrium.

For increasing gap fields, the peak of the current rollover moves to earlier times, as seen in Fig. 3.7(a) and in more detail in Fig. 3.8(a), for the 8-pulse (no initial plasma) sequence. At the highest fields, the rollover peak moves toward ~5 μs, a range consistent with the few microsecond delays for the deepest channels in Fig. 3.2(b). This is consistent with our observation that as the gap field increases, the deepest channels occur at earlier times.

A rough estimate of the current decay timescale after the rollover is simply the time for thermal diffusion to double the radius of the initial laser-induced channel, $\tau_{decay} \sim R^2/4\alpha$ [50], where $\alpha = 0.19\ \mathrm{cm}^2/\mathrm{s}$ is the thermal diffusivity of room temperature air [104] and we use $R = 100$ μm as twice the initial channel radius. This gives $\tau_{decay} \sim 130$μs, of the same scale as in Fig. 3.7(a).

Fig. 3.7(b) plots the total charge $Q_{gap} = \int_0^\infty I_{gap}(t)dt$ as a function of gap voltage for the single pulse (plasma) and 8-pulse (plasma-free) gap excitations of Fig. 3.7(a), with the curves terminating at breakdown. Here it clear that the pre-breakdown charge driven across the gap increases with gap field, largely owing to electrode-supplied carriers traversing the increasingly conductive air channel. While the charge driven in the initial plasma-free laser excitation case (green curve) is somewhat lower than the initial plasma case (blue curve), the curves converge near breakdown. Measurements of Q_{gap} enable an extreme upper estimate of average electron density $\overline{N_e}$ in the gap during the current pulse: $Q_{gap} \sim \overline{N_e}\pi a^2 L_{gap}$, where $a \sim 50$ μm is the approximate air channel radius (see Fig. 3.2(b)) and $L_{gap} = 4$ mm is the gap spacing. Using the plot maximum $Q_{gap} \sim 20$ pC gives $\overline{N_e} \sim 4 \times 10^{12}\ \mathrm{cm}^{-3}$. This is orders of magnitude lower than the electron density generated in our femtosecond filaments

(see Fig. 3.5(b)), further supporting the picture that electrons from the filament plasma contribute little *directly* to these current pulses.

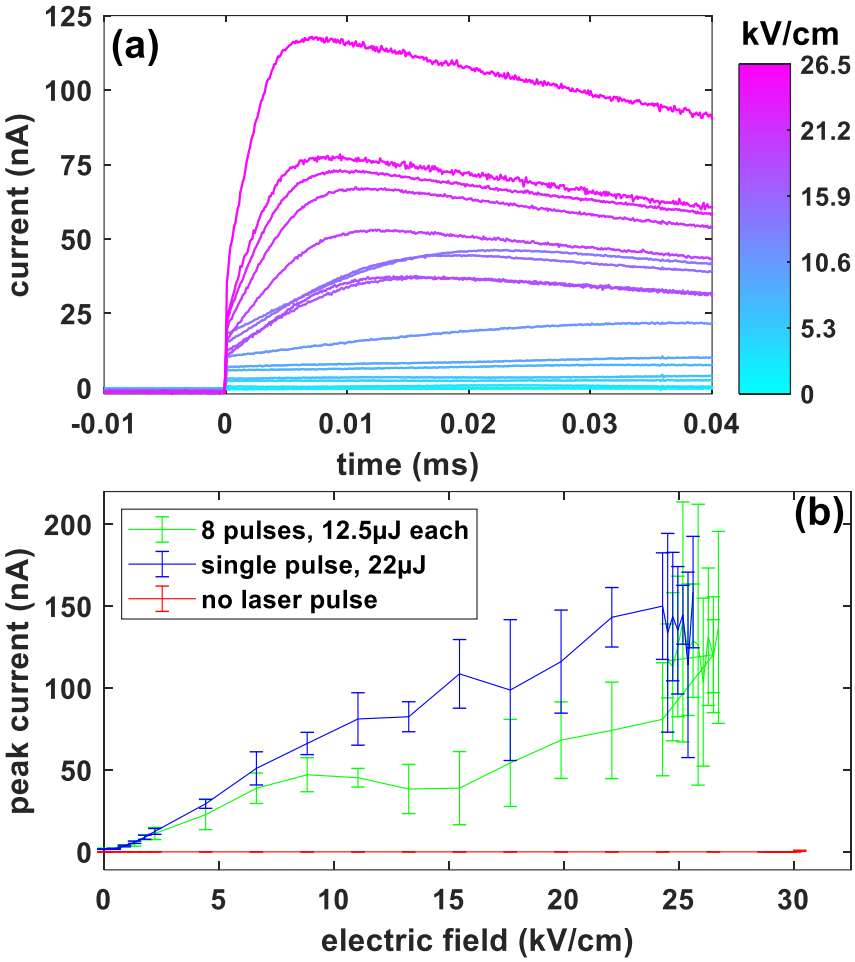

Figure 3.8 Current measurements (below the breakdown threshold) using the green-boxed current monitor depicted in Fig. 3.1(a). **(a)** Transient gap current vs gap field induced by the 8-pulse (12.5μJ, 100 fs, no plasma) sequence. **(b)** Peak gap current vs. gap voltage below the breakdown threshold for the single pulse (blue, plasma) and 8-pulse (green, no plasma) cases. The blue and green curves converge and terminate where breakdown occurs at ~25 kV/cm. The no-laser case (red) is shown for comparison; breakdown occurs near ~30 kV/cm.

Fig. 3.8(b) shows the peak current using the two sets of laser parameters of Fig. 3.3 and Fig. 3.7 giving initial plasma (blue curve) and negligible initial plasma (green curve). As discussed earlier, the pulse energies were chosen so that the initial density depression was $\Delta N/N_0 \sim 3\%$ for each case. A laser-free curve (red) is plotted for comparison, where below breakdown, the current is zero. As in the case for total

charge (Fig. 3.7(b)), the peak current for the single pulse case increases vs. gap field more than in the 8-pulse case, owing to its higher initial electron density and increased electrode-driven air heating and channel depth (as seen in Fig. 3.6). Even though the 8-pulse train generates less than ~1% of the electron density of the single pulse (see earlier discussion), the peak current is roughly 50% of the single pulse case until they converge when the gap voltage is close to the breakdown threshold. This again strongly suggests that the main role of the laser—whether through generating filament plasma or by rotational excitation—is to initially heat the air and increase the density hole or channel depth to provide enhanced channel conductance; thereafter, free carriers are largely supplied by the gap electrode. In both cases, at sufficiently high gap voltage, the carriers increase in number owing to impact ionization and continue to resistively heat the gas, increasing the density hole volume and conductance. Just before breakdown, the currents are comparable (Fig. 3.8(b)) as are the density hole volumes (Fig. 3.3).

3.5 Summary

We have measured the spatial and temporal dynamics of air heating in an ultrashort laser-triggered spark gap prior to breakdown. We find that once a reduced density air channel is created between the electrodes, regardless of how it was formed, it acts as a preferred channel through which subsequent gap field-driven current may flow. This current further resistively heats the channel, deepening it and increasing conductance and current, leading to eventual breakdown for sufficient gap field. Below the breakdown threshold field, laser-triggered current transients in the

gap decay as the air depression channel becomes shallower and wider from transverse thermal diffusion.

To elucidate the relative roles of the plasma and the air density depression channel (density hole) induced by the laser, we performed gap current measurements and longitudinal interferometry through the gap electrodes. In the case of plasma and density hole generation by a single filamenting pulse, the electrons are initially driven by the gap field and further heat the air and deepen the depression channel, with subsequent current provided by the electrodes and channeled through the density hole. In the case of little plasma but comparable density hole generation from an 8-pulse sequence, the lower current initially provided by the electrodes is preferentially channeled through the density hole, heating it further. As gap voltage is increased, impact ionization increases the gap current to the point where the current and the density hole volume in both cases are comparable. This leads to similar breakdown thresholds. Below the breakdown threshold, laser excitation of the gap triggers an electrode-supplied current transient through the reduced density channel. As the channel widens and decreases in depth due to transverse thermal diffusion, the current decays on the thermal diffusion time scale of $\sim 100\ \mu s$ and the air gap returns to a non-conducting equilibrium.

For ease of diagnostic access, we examined relatively short spark gaps; however, we expect the scenario we described here to apply to longer femtosecond filament-triggered discharges; its range of applicability will be the subject of future experiments.

Chapter 4: 100 m scale air waveguides from LG beam filaments

As presented in Chapter 2, laser filamentation in air leads to energy deposition in long and narrow channels with aspect ratios inaccessible to linear focusing geometries. Chapter 3 showed applications of centimeter scale energy deposition regions to trigger high voltage spark gaps. Deposition from multiple filaments over ~1 m has already been demonstrated to generate air waveguides in 2014 [6]. This Chapter will present a beam forming approach to generate air waveguides approaching 100 m length scales.

4.1 Introduction

Air waveguides have been generated by modifying the refractive index of air in a controlled manner to produce an ambient air density channel surrounded by a cladding of reduced density. This reduction in density is generated by locally heating the air, resulting in decreased density once pressure equilibrium is reestablished. Air heating using only linear absorption limits the length of the heated region through diffraction; laser filaments can maintain tight focus over many Rayleigh lengths and overcome this limitation. Filamentation is a nonlinear propagation process experienced by high intensity laser beams in a transparent media such as air. During filamentation in air a laser pulse experiences a balance between Kerr self-focusing and plasma defocusing, generating a ~100 μm diameter beam core lasting for many Rayleigh lengths surrounded by a lower intensity reservoir [8]. Air is heated in the

wake of a filament primarily due to plasma recombination and relaxation of molecular rotational states that were excited by the laser's electric field [2].

Single filamentation deposits energy over a small transverse area and extended length, while waveguide generation additionally requires fine control over the transverse profile. Prior experiments used a binary phase mask to produce an approximate TEM_{11} mode, generating four individual filaments with an undisturbed region of air in the center capable of guiding [6]. Other works have studied filament array generation with amplitude masks or binary phase masks [105,106]. In this Chapter we demonstrate the use of an LG_{01} beam to generate a ring of filaments [107,108]. This structure provides energy deposition in the necessary structure for waveguiding and the number of filaments automatically scales with beam size provided fluence remains constant. We use a helium cell diagnostic to study the evolution of the guided mode over 8 m in the lab and have demonstrated guiding over 40 m down a hallway [59].

4.2 Generating air waveguides

The experimental setup for lab scale guiding is shown in Fig. 4.1. The goal of these experiments was to check the feasibility of using an LG beam to generate waveguides rather than modes with discrete intensity lobes. Measurements were made of the guided mode evolution inside the air waveguide as function of propagation distance, and are complemented by axially resolved measurements of the energy deposition profile responsible for generating the waveguide. The filaments for the waveguide were generated using a high power chirped pulse amplification

Ti:Sapphire laser system operating at a 10 Hz repetition rate with a central wavelength $\lambda_0 = 800$ nm. The minimum pulse duration for the laser system is 45 fs (FWHM), but 100 fs pulses were used for most of the experiments by adjusting the grating spacing inside the Treacy compressor [109]. Post compression energies of up to 120 mJ were used with energy controlled by a λ/2 waveplate and reflection from a thin film polarizer (TFP). To generate the appropriate spatial distribution of filaments for waveguiding, the pre-compressor laser beam was transmitted through a 16 step spiral phase plate and spatially filtered to produce an LG_{01} beam. After compression a $3\times$ reflective down-collimating telescope produced a 4.5 mm diameter LG ring which started filamenting within 1 m of propagation and had small hot spots on burn paper indicative of filament cores until the end of the lab 8 m downstream.

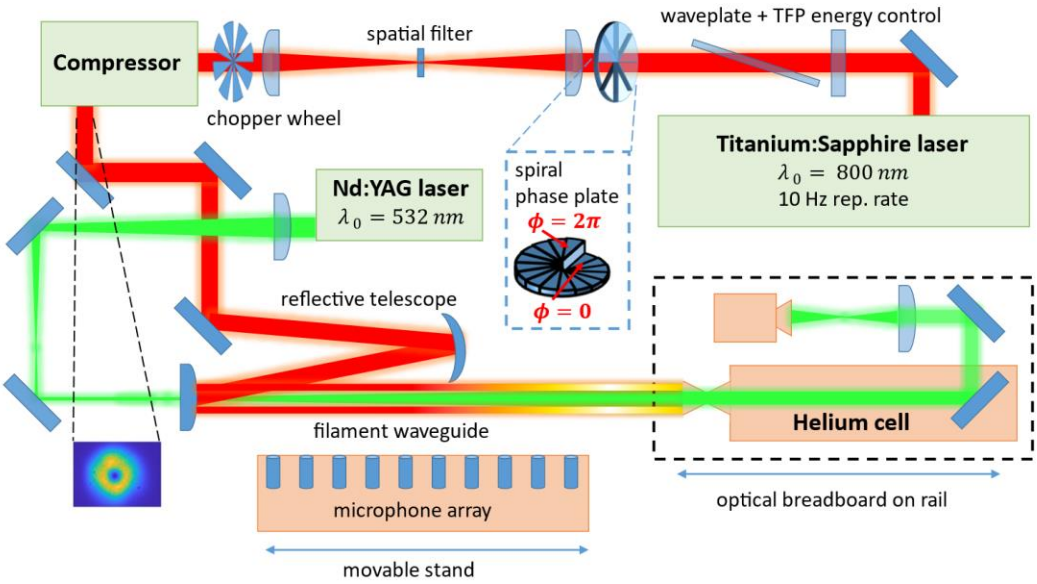

Figure 4.1 Experimental setup for measuring air waveguide profiles and observing the guided mode evolution over 8 m of propagation in the lab.

Lab-based experiments over 8 m are first studied with a range of diagnostics before presenting evidence of guiding spanning the length of a 40 m hallway. A

microphone array composed of 64 synchronized microphones over 126 cm was used to map out energy deposition profiles of the filament waveguides as shown in Fig 4.2(a). A single cycle acoustic wave is formed after energy deposition from a filament heats the air and generates a local pressure increase [3]. The amplitude of the acoustic signal is proportional to energy deposited, which drives initial density hole generation and is a good metric of the air waveguide index contrast [1]. 100 laser shots were averaged at each of the eight microphone array positions and scaled by +-5% to account for slight differences in radial position. Measured energy deposition climbs rapidly starting 50 cm from the reflective telescope and persists for ~2 m, with a long decay afterwards. A similar trend observed in previous works [2] attributed the high energy deposition region to plasma generation and heating whereas the long tail was attributed to rotational heating. Transverse waveguide profile measurements were done using burn paper. Sample images are provided in Fig. 4.2(b) at a distance of 1 m, 4 m, and 7 m after the reflective telescope showing an initial solid ring of high intensity which then breaks apart into 20–30 individual filaments. This would imply the energy in each filament is ~3 mJ, or 8 P_{crit} at 100 fs, approximately the maximum

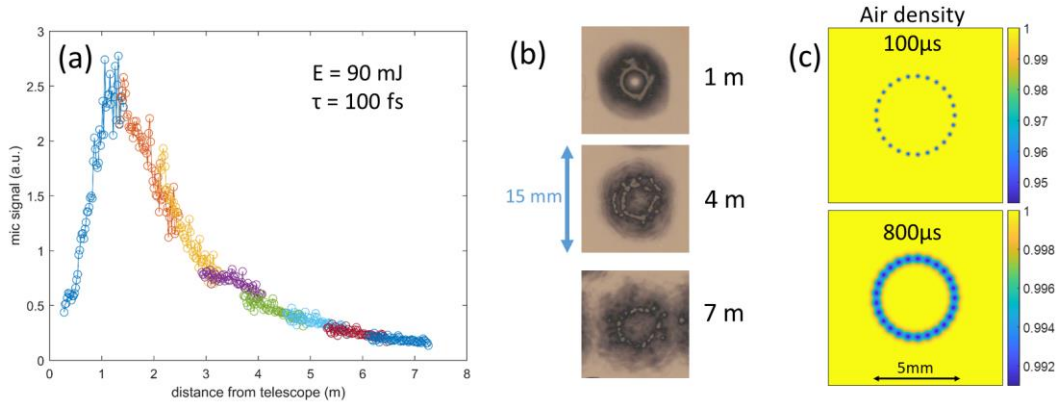

Figure 4.2 (a) Energy deposition profile and **(b)** burn paper of 4.5 mm diameter LG_{01} waveguide produced using 100 fs pulse duration and 90 mJ of energy. **(c)** Simulated density hole profile from 25 filaments evenly spaced on the circumference of a 4.5 mm diameter ring after 100 µs and 800 µs of thermal diffusion.

that has been seen in a single filament before it splits into multi-filamentation [110].

4.3 Guiding over 8 m

Having confirmed that both the longitudinal and transverse energy deposition profile of a filamenting LG beam is conducive to generating air waveguides we move on to experimental verification of guiding. Guiding efficacy was tested using a frequency-doubled pulsed Nd:YAG laser. A digital delay generator synchronized the probe beam to the filamenting beam and allowed variable delay such that energy deposited by each individual filament had time to diffuse into a continuous low-density moat before injecting of the beam to be guided. It has been previously shown that beyond the first 10 μs linear thermal diffusion accurately models the evolution of the atmospheric density hole according to the following equation: $\Delta N(r,t) = N_b \Delta T\,(T_b + \Delta T)^{-1}(R_0^2/(R_0^2 + 4\,\alpha t\,))\exp\,(-r^2/\,(R_0^2 + 4\,\alpha t\,))$ [50]. With N_b and T_b being the ambient density and temperature. The initial energy deposition is taken to be a Gaussian with 1/e radius $R_0 = 50$ μm and temperature increase $\Delta T = 100$ K which matches typical filament conditions [50,111]. Fig. 4.2(c) shows that with these initial conditions and 25 filaments spread uniformly on a 4.5 mm diameter ring, individual density holes are clearly visible at 100 μs, but merge into a solid ring after 800 μs with an approximately 1% peak density hole depth, this is mirrored in experiments where an 800 μs probe delay was found to provide good guiding and was used for the 8 m guiding experiments. The 532 nm beam was coupled into the waveguide by transmitting through the dielectric curved mirror of the 800 nm reflective telescope. The probe beam was diverging with a Rayleigh length of

$z_r \sim 60cm$, or the equivalent of focusing with a ~ f / 950 geometry. This beam geometry provided a more rigorous test of the waveguide than a collimated probe would and allowed us to demonstrate guiding over ~13 z_r in the lab and nearly 70 z_r in the hallway. The $\theta \sim 0.53$ mrad probe divergence angle is several times smaller than the maximum acceptance angle for a step index fiber with ambient air as the core and 0.995 atm density air as the cladding.

The guided beam was directly imaged onto a CMOS camera; co-propagating filament supercontinuum was attenuated using a 532 nm bandpass filter and linear polarizer, the camera exposure was also temporally gated to eliminate any residual supercontinuum light. Previous air waveguide experiments relied on geometric focusing to initiate filamentation which allowed safe imaging of the guided beam after geometric defocusing terminated filamentation [6]. In the setup demonstrated here the filamenting beam is collimated and maintains high intensity until the end of the lab. To image the guided beam in such conditions without damaging optics, a helium cell was used [59]. This is a compact chamber filled with helium and a converging-diverging nozzle opening at the front. The filament waveguide enters through the nozzle and halts filamentation due to lower n_2 of helium compared to air. After linearly propagating and diffracting for 70 cm an uncoated beam sampler is used to attenuate the beam ensuring filamentation doesn't resume after exiting the helium cell. This assembly of helium cell and imaging optics was mounted on a 2 meter long rail allowing imaging of the guided beam at different propagation distances.

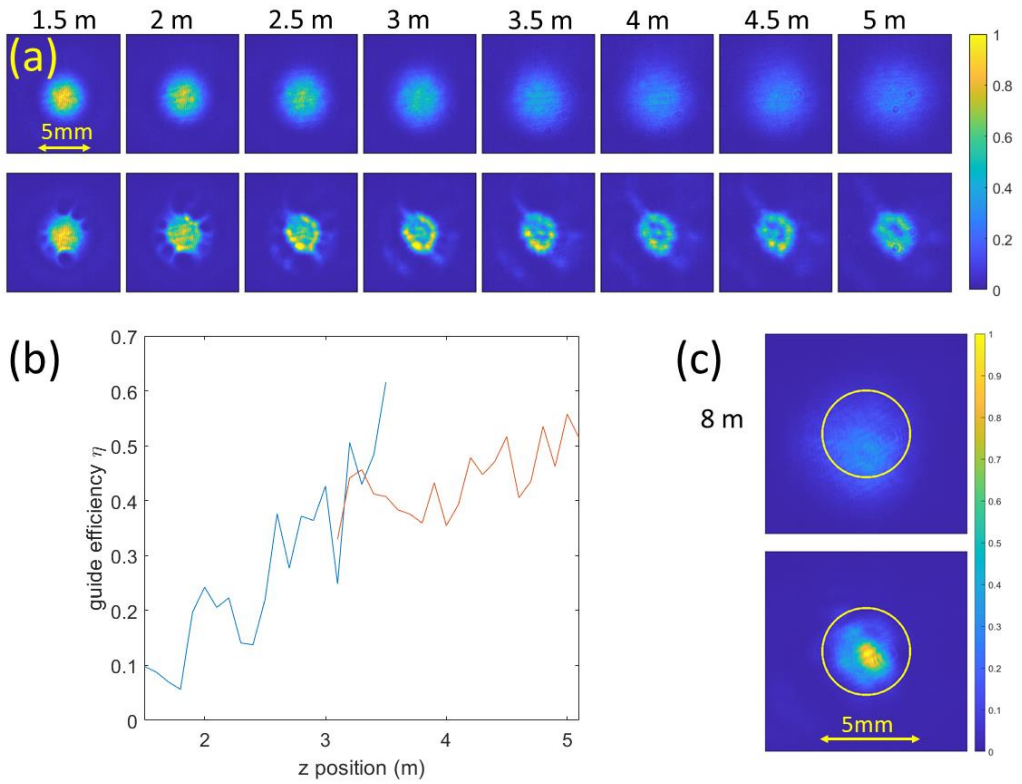

Figure 4.3 532 nm probe beam guided by an air waveguide formed by a 4.5 mm diameter LG_{01} beam with 100 fs pulse duration and 90 mJ of energy. **(a)** 50 shot average images of unguided (top row) and guided (bottom row) probe beam at various propagation distances and 800 μs probe delay. **(b)** Guiding efficiency for the corresponding data with a 4.2 mm diameter central mode. **(c)** End-of-lab images after 8 m of propagation with 4.2 mm diameter central mode area indicated by a circle.

For a 4.5 mm diameter LG beam with 90 mJ of energy and a 100 fs FWHM pulse duration, guiding is clearly visible in Fig. 4.3 (a), the unguided beam rapidly diverges whereas with a waveguide the probe beam maintained a fixed ~4 mm diameter spot size. These images were produced by inserting a chopper into the 800 nm beam so every other probe laser pulse was guided. 100 consecutive images were saved for every propagation distance presented in Fig 4.3 and the average of 50 guided and 50 unguided laser shots is displayed. A quantitative wave guide quality metric used in previous work is 'guiding efficiency' defined as:

$$\eta = (E_g - E_{ug}) / (E_{tot} - E_{ug}) \quad (4.1)$$

where E_g and E_{ug} are the energy within the central mode area with and without

waveguide respectively, and E_{tot} is the total beam energy [6]. This parameter η scales from 0 to 1 and shows the fraction of energy retained within the waveguide that would otherwise diffract from within the central mode area under linear propagation. Fig. 4.3 (b) shows guiding efficiency calculated with a 4.2 mm diameter central mode which contained the high intensity guided section as seen in Fig 4.3 (b). A guiding efficiency value as high as 50 % was obtained after 5 m, comparable to what was achieved over 70 cm with a TEM_{11} mode in previous works [6]. We have now demonstrated that by using a collimated LG_{01} beam we can generate an air waveguide that is an order of magnitude longer and wider than previously achieved with a TEM_{11} beam while still maintaining comparable guiding efficiency.

4.4 Guiding over 40 m

Having demonstrated guiding over the full 8 m length of the lab with a filamenting LG beam we next demonstrate the effect of guiding over 40 m in a hallway adjacent to the lab. Images of burn paper in Fig. 4.4(a) do not show hot spots indicative of filament cores after 20 m of propagation with laser parameters similar to

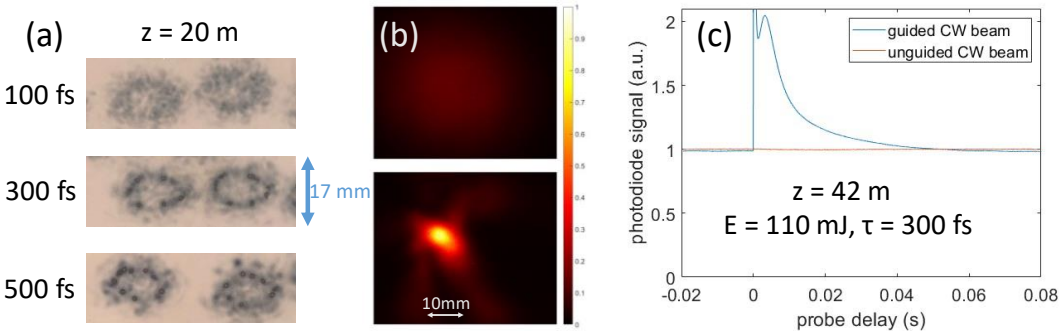

Figure 4.4 Guiding results after 40 m of propagation. **(a)** burn paper showing increased intensity at 20 m with increasing pulse duration (70, 90, 120 mJ at 100, 300, 500 fs). **(b)** Guided mode after 40 m with a 300 fs 110 mJ beam and 5 ms probe delay. **(c)** probe power within a 12.5 mm aperture as a function of probe delay.

those used in lab guiding experiments. In an effort to extend filamentation, three modifications were made. Beam size was increased slightly lowering diffraction, this allowed an increase of energy up to 120 mJ (without damage to the compressor gratings) and a longer pulse duration was used. The 6 mm diameter final beam size had a Rayleigh length of ~35 m, comparable to the length of the hallway. With the additional energy, a longer pulse duration was tested, generating longer filaments. Fig 4.4(a) shows the spatial characterization of the beam on burn paper after 20 m of propagation, demonstrating that higher intensity is maintained over longer propagation distance when filaments are initiated using 300 fs pulse duration compared to 100 fs. The setup used to initiate filamentation and couple in the probe beam was identical to the one used in the lab. The helium cell was not able to be used for imaging due to the large probe size after 40 m of divergent propagation. Instead, imaging of the guided mode in our hallway propagation range was performed using a camera and bandpass filter, imaging the guided beam after scattering from an alumina beam-stop. This technique has lower imaging fidelity than direct imaging, but still clearly shows the effect of guiding in Fig. 4.4 (b).

Probe injection delays on the order of 3–5 ms provided the best observed guiding over the larger distances. This contrasts with previous results of <~1ms; the larger optimal probe delay may be explained by the larger LG ring and a smaller number of filaments at longer pulse durations. Both of these differences would require additional diffusion time before formation of a uniform low-density ring. In order to observe the temporal dynamics of waveguiding, the pulsed probe laser was replaced with a 100 mW CW 532 nm laser diode. An integrating sphere fitted with a

silicon photodiode at the end of the hallway propagation range measured power within the central mode area as a function of time, allowing for the temporally-resolved guiding observation shown in Fig. 4.4 (c). The central mode area used was 12.5 mm diameter, corresponding to the input aperture of the integrating sphere to which the photodiode was mounted. Effective guiding over 40 m is observed for probe delays in the range of 1–15 ms, and some evidence of guiding is still visible at 40 ms. Waveguiding at long probe delays is very promising for generating steady state waveguides; a higher repetition rate laser could be used to produce a quasi-steady-state gas density depression.

4.5 Conclusion

It has been demonstrated that a function air waveguide can be created by using an LG_{01} beam to generate an optimized pattern of filaments spread around a ring. Guiding was demonstrated over 8 m with a guiding efficiency comparable to that first demonstrated over 1 m [6]. It was also shown that with longer pulse durations, guiding is feasible over the full length of a 40 m hallway paving the way for guiding over hundreds of meters. Given that the guiding effect is observed for probe injection delays up to ~50 ms for the hallway experiments, a 20 Hz laser might be sufficient to generate a quasi-steady state waveguide. Further studies are needed to measure what laser parameters are needed to produce 100 m or 1 km length air waveguides. Beam size can be scaled up to further decrease diffraction, but the relationship between filament length and pulse duration are not yet fully understood.

Chapter 5: Filament fog clearing

In Chapter 4 it was demonstrated how filaments can be utilized to increase signal transmission through clear air by generating a long-lasting thermal waveguide. However, transmission through air is often reduced due to the presence of aerosols such as dust or fog. In those scenarios aerosol mitigation may play a bigger role in increasing signal transmission. The use of lasers to clear fog has been proposed and demonstrated as early as 1968 [112]. These early experiments relied on direct optical heating to vaporize droplets and clear a transparent path through the fog. More recent works have suggested that filament self-focusing and self-healing properties may clear longer channels through fog [113]. This chapter will briefly review work done in the ILMI in collaboration with Swiss researchers from the research group of J. P. Wolf [114] and follow up experiments led by Andrew Goffin [115] related to fog clearing using a filament.

5.1 Introduction

As described previously laser filaments are a self-sustaining light structure formed by ultrashort pulses. For an 800 nm beam in air filaments typically have a core diameter of $d_{core} \sim 100\,\mu$m and can last for hundreds of meters [116]. Filaments self-focus to high intensities ($10 - 100$ TW/cm^2) which generates a low-density plasma. Recombination of plasma leads to rapid pressure increase in air driving a single cycle cylindrical acoustic wave [3,6,50,117,118]. Over 0.1 – 1 ms the deposited thermal energy is present as an expanding reduced air density channel

much wider than the filament core [50,64,117–119]. It has been shown that a laser filament can clear a channel through fog [120,121] with the speculated mechanism being drop motion induced by the sound wave emitted from the filament. This acoustic wave can alternatively be generated by resonantly driving rotational excitations of air molecules with a train of pulses. For nitrogen molecules a study using four pulses showed nearly a $2\times$ enhancement of heating with inter-pulse delay on resonance at 8.36 ps compared to off resonance at 8.66 ps [5].

5.2 Fog clearing experiment

Fog clearing was tested in laboratory environments by using an ultrasonic humidifier to fill a 'cloud chamber' with water droplets. This method generates a distribution of droplet sizes with a mean value around 5 μm radius (measured by a Grimm 1.109 particle sizer), a size commonly found in natural fog [122]. The experimental setup used a 10 cm long chamber with droplet density as high as 1.5×10^5 cm^{-3} corresponding to an attenuation of -10 dB for the $\lambda = 1.55$ μm telecom laser diode used as a probe. Previous works have shown that due to their self-healing properties filament propagation is not impacted by drop densities as high as $N_d \sim 10^5$ cm^{-3} [113,123,124].

The purpose of the experiment presented here was to demonstrate clearing of fog using a train of lower energy pulses where rotational excitations are the main energy deposition mechanism. The driving laser was a 1 kHz repetition rate Ti:Sapphire laser with a central wavelength $\lambda_0 = 800$ nm focused by a 1 m lens at $f/80$. The total laser energy of 3.8 mJ was separated into 8 pulses with variable

temporal spacing using a 'pulse stacker' nested Michelson interferometer [100]. Two pulse delay configurations were compared, maximum heating was achieved by setting the delay between pulses at 8.36 ps, and lower heating at the same laser intensity was achieved at 8.66 ps delay between pulses.

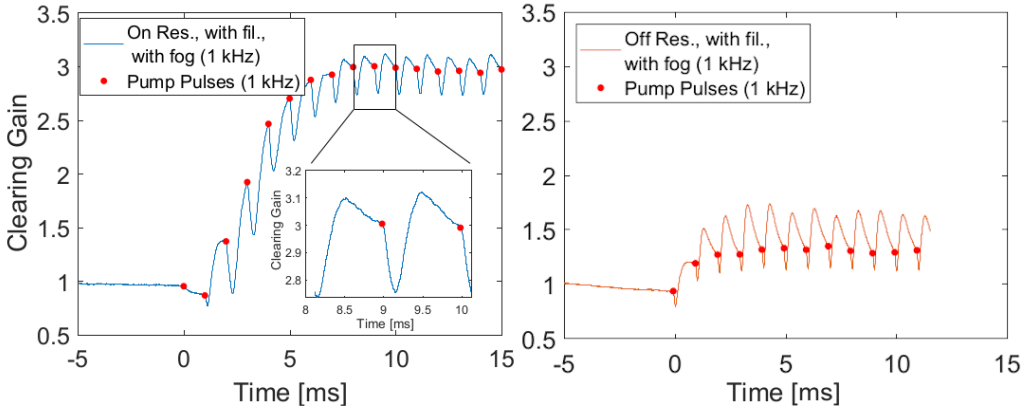

Figure 5.1 Change in transmitted power through fog from 8 pulses resonantly driving rotational excitations (left) or off resonance (right) after the laser is unblocked at t = 0 ms. Total laser energy is 3.8 mJ with a fog droplet density of $1.3 \times 10^5 cm^{-3}$ when on resonance and of $0.7 \times 10^5 cm^{-3}$ when off resonance.

Fog transmission was tested with a $\lambda = 1.55$ μm laser diode counter-propagating relative to the filament by transmitting through 800 nm dielectric mirrors. The probe beam was focused into the cleared region by an $f = 1$ m lens with the transmitted power recorded on a photodiode and oscilloscope. The power was recorded with unperturbed fog before unblocking the 800 nm beam. Fig. 5.1 above shows the proportional transmission increase and demonstrates how several 800 nm laser shots are required to clear the fog. Immediately after each laser shot the slight dip in transmission is attributed to the air thermal profile refracting the probe. This is followed by an increase in transmission as the fog is cleared. Note that at all times between laser shots the transmission stays above that for unperturbed fog indicating that a 1 kHz repetition rate laser clears a steady state open channel through fog.

Tuning the time delay between pulses to be off resonance still provides a fog clearing effect, but a significantly weaker one with only 1.7 dB signal increase compared to 4.8 dB for the on resonance case. Since in both cases the energy and pulse duration for the laser pulses are identical it appears that energy deposition plays an important role for fog clearing in this experimental setup.

5.3 Individual drop interaction

The previous experiment highlighted the importance of laser energy deposited for fog clearing, however the exact mechanism through which deposited energy clears droplets was still not fully understood. A second set of experiments was devised to study laser interaction with a single water droplet precisely positioned near a filament rather than a region of fog. The goal of these experiments was twofold; observe the interaction of a water droplet with an acoustic wave from a filament and verify the minimal distance between a droplet and filament before optical interaction shatters the droplet.

A single 5 μm radius droplet was generated by a 'droplet on demand' system consisting of a triggerable waveform generator, a high-speed amplifier, and a piezo driven micro dropper nozzle with a 10 μm inner diameter nozzle. The dropper apparatus was mounted on a 3-axis translation stage allowing fine control over initial droplet position relative to the filament. The droplet trigger was synchronized to a $\lambda = 800$ nm Ti:Sapphire laser which generated the filaments and a $\lambda = 532$ nm frequency doubled Nd:YAG laser used as a probe. The probe was used both for

imaging droplet displacement after a controlled delay and measuring filament energy deposition by interferometrically observing the cumulative air density depression [1].

The first optical setup generated a filament from a collimated beam with $w_0 = 1$ mm waist ($1/e^2$ intensity radius), 2.8 mJ of energy, and a $\tau = 45$ fs temporal FWHM. The probe laser was used to image the droplets at 500 μs delay after the filament while initial drop-filament separation was scanned. For initial distances less than 150 μm from the filament core center drops were no longer visible after 500 μs. Images at 0.1 μs delay showed the droplet exploding, indicating that for a filament with these parameters any drops closer than 150 μm are shattered, presumably by optical interactions. Comparing the initial drop position to the position at 500 μs delay, no radial movement was observed at any initial position for which the drop was not shattered.

A second optical setup was used to diagnose the interaction of a droplet with an acoustic wave in a scenario where optical interaction was artificially reduced. In this setup the same Ti:Sapphire laser was attenuated to 100 – 500 μJ and was focused at $f/120$. The focused beam with a diameter $2\,w_0 \sim 100$ μm is similar in size to a filament core, but without the large energy reservoir typical of a filament. Using longitudinal interferometry, the phase shift due to air density change was measured. This density change was driven by energy deposition from the laser. By integrating over the full measurement area a total energy deposition per unit length was obtained. For a pump energy of 450 μJ air heating corresponding to 4.8 μJ / cm energy deposition was obtained, somewhat higher than the 3.5 μJ / cm that was previously measured using the same technique for a typical air filament [1].

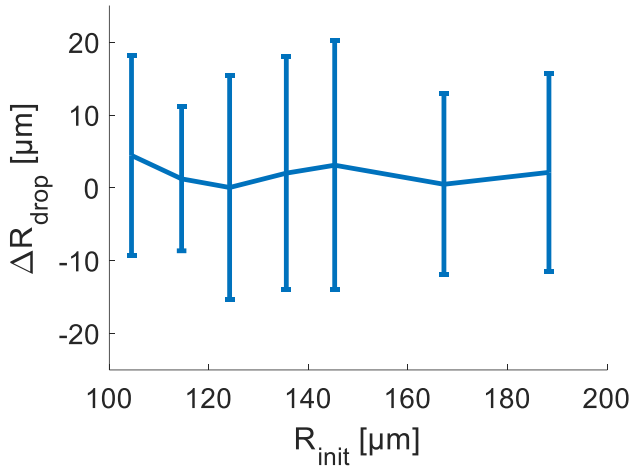

Figure 5.2 Radial drop displacement away from the filament core as a function of initial position after 500 μs with a 450 μJ pump energy. Error bars represent ± one standard deviation over 100 shots. Below 100 μm initial position the drops are all shattered by optical interaction.

With the pump laser set to 450 μJ the droplet initial position was once again scanned relative to the center of the laser beam. With the focused laser beam the drop was able to be moved as close as 100 μm before shattering. Since energy deposition is similar to the collimated case, but the shattering radius is decreased, optical interactions must be the mechanism of shattering. Even with this closer minimal spacing almost no drop movement was observed. For 100 samples with droplet initial position in the range of 100 – 110 μm the average recorded drop movement ΔR was less than 5 μm after 500 μs. This drop displacement was less than the natural spread in initial drop position which is the primary source of error bars in the above figure.

The conclusion from these two experiments is that the acoustic wave produced by a typical 800 nm filament in air is insufficient to move water droplets. At 100 μm initial separation, a displacement of less than 5 μm over 500 μs is observed, however for a collimated beam that forms a filament all drops closer than 150 μm are shattered. The potential for acoustic clearing of fog still exists for higher energy

deposition scenarios. Tightly focused high energy filaments can produce significantly higher plasma densities and energy depositions. Alternatively, resonantly driven rotations of air molecules, as used in section 5.2, can also produce a large amount of heating [5]. Finally, filaments at different wavelengths, such as a 10.6 μm 'megafilament' [25], or longer pulse durations [46] may increase plasma heating and offer a promising approach for long range fog clearing.

Chapter 6: Conclusion and future work

6.1 Summary

Laser filamentation is a phenomenon that has been observed in solids since the development of pulsed lasers. The advent of chirped pulse amplification opened the field of study of filamentation in gasses, most importantly air. The study of filamentation can broadly be divided into a study of how the laser pulse evolves and how gas responds to a filament. This thesis has documented work to study the evolution of air after a filament and numerous applications thereof.

In Chapter 2 a new method for measuring the energy deposition profile of a single pulse using an array of microphones has been demonstrated and applied to show the importance of air turbulence on filamentation over laboratory length scales. Air heating either by a filament plasma or resonantly driven air molecular rotations was studied in Chapter 3 as a method to trigger high voltage spark gaps. By observing the influence of initial plasma density on the evolution of pre-breakdown gas density an understanding was developed of the air heating mechanism between two high voltage electrodes. In Chapter 4 an application of structured multi-filamentation from an initial LG_{01} beam profile was shown to generate waveguides over tens of meters, more than an order of magnitude longer than previous demonstrations. Chapter 5 used a similar heating mechanism as Chapter 3 to show that rotational air heating can clear channels through fog. A follow up experiment with a single drop showed that for a collimated filament, the single cycle acoustic wave which results from filament

energy deposition is insufficient to move drops and fog clearing is primarily driven by optical shattering.

6.2 Future and ongoing work

The microphone array used for the collapse locations measurements presented in Chapter 2 is a unique measurement tool that has not been fully utilized yet. Andrew Goffin is now leading a study into filament length as a function of pulse duration. For air waveguide experiments in Chapter 4 a pulse duration >200 fs was found to improve guiding over large distances. Measurements with the microphone array will inform us if there is an optimal pulse duration for maximized total energy deposition or energy deposition per unit length.

Waveguiding results in Chapter 4 with a CW probe showed guiding over a surprisingly long temporal window. Whereas previous results over 1 m showed the waveguide thermal profile to dissipate over ~1 ms the long range waveguide lasted for more than 20 ms. This shows promise for generating a quasi-steady state waveguide using a higher repetition rate laser system. A 10 mJ, 1 kHz rate system available in the lab is sufficient to generate four filaments or commercial thin disk Yb:YAG systems can produce >200 mJ pulses at 1 kHz with a ~1 ps pulse duration potentially generating long range waveguides capable of guiding a CW laser and overcoming thermal blooming.

Bibliography

1. E. W. Rosenthal, N. Jhajj, I. Larkin, S. Zahedpour, J. K. Wahlstrand, and H. M. Milchberg, "Energy deposition of single femtosecond filaments in the atmosphere," Opt. Lett. **41**, 3908–3911 (2016).
2. E. W. Rosenthal, J. P. Palastro, N. Jhajj, S. Zahedpour, J. K. Wahlstrand, and H. M. Milchberg, "Sensitivity of propagation and energy deposition in femtosecond filamentation to the nonlinear refractive index," J. Phys. B **48**, 094011 (2015).
3. J. K. Wahlstrand, N. Jhajj, E. W. Rosenthal, S. Zahedpour, and H. M. Milchberg, "Direct imaging of the acoustic waves generated by femtosecond filaments in air," Opt. Lett. **39**, 1290–1293 (2014).
4. N. Jhajj, Y.-H. Cheng, J. K. Wahlstrand, and H. M. Milchberg, "Optical beam dynamics in a gas repetitively heated by femtosecond filaments," Opt. Express **21**, 28980–28986 (2013).
5. S. Zahedpour, J. K. Wahlstrand, and H. M. Milchberg, "Quantum Control of Molecular Gas Hydrodynamics," Phys. Rev. Lett. **112**, 143601 (2014).
6. N. Jhajj, E. W. Rosenthal, R. Birnbaum, J. K. Wahlstrand, and H. M. Milchberg, "Demonstration of Long-Lived High-Power Optical Waveguides in Air," Phys. Rev. X **4**, 011027 (2014).
7. E. W. Rosenthal, N. Jhajj, J. K. Wahlstrand, and H. M. Milchberg, "Collection of remote optical signals by air waveguides," Optica **1**, 5–9 (2014).
8. A. Couairon and A. Mysyrowicz, "Femtosecond filamentation in transparent media," Phys. Rep. **441**, 47–189 (2007).
9. A. Ting, I. Alexeev, D. Gordon, R. Fischer, D. Kaganovich, T. Jones, E. Briscoe, J. Peñano, R. Hubbard, and P. Sprangle, "Measurements of intense femtosecond laser pulse propagation in air," Phys. Plasmas **12**, 056705 (2005).
10. R. Y. Chiao, E. Garmire, and C. H. Townes, "Self-Trapping of Optical Beams," Phys. Rev. Lett. **13**, 479–482 (1964).
11. P. Polynkin and M. Kolesik, "Critical power for self-focusing in the case of ultrashort laser pulses," Phys. Rev. A **87**, 053829 (2013).
12. J. H. Marburger, "Self-focusing: Theory," Prog. Quantum Electron. **4**, 35–110 (1975).
13. G. Fibich and A. L. Gaeta, "Critical power for self-focusing in bulk media and in hollow waveguides," Opt. Lett. **25**, 335–337 (2000).
14. S. Zahedpour, J. K. Wahlstrand, and H. M. Milchberg, "Measurement of the nonlinear refractive index of air constituents at mid-infrared wavelengths," Opt. Lett. **40**, 5794–5797 (2015).
15. D. Milam, "Review and assessment of measured values of the nonlinear refractive-index coefficient of fused silica," Appl. Opt. **37**, 546–550 (1998).
16. D. Strickland and G. Mourou, "Compression of amplified chirped optical pulses," Opt. Commun. **56**, 219–221 (1985).
17. B. Rus, P. Bakule, D. Kramer, G. Korn, J. T. Green, J. Nóvak, M. Fibrich, F. Batysta, J. Thoma, J. Naylon, T. Mazanec, M. Vítek, R. Barros, E. Koutris, J. Hřebíček, J. Polan, R. Baše, P. Homer, M. Košelja, T. Havlíček, A. Honsa, M.

Novák, C. Zervos, P. Korous, M. Laub, and J. Houžvička, "ELI-Beamlines laser systems: status and design options," in *High-Power, High-Energy, and High-Intensity Laser Technology; and Research Using Extreme Light: Entering New Frontiers with Petawatt-Class Lasers* (SPIE, 2013), Vol. 8780, pp. 265–276.

18. A. Braun, G. Korn, X. Liu, D. Du, J. Squier, and G. Mourou, "Self-channeling of high-peak-power femtosecond laser pulses in air," Opt. Lett. **20**, 73–75 (1995).
19. H. Wille, M. Rodriguez, J. Kasparian, D. Mondelain, J. Yu, A. Mysyrowicz, R. Sauerbrey, J. P. Wolf, and L. Wöste, "Teramobile: A mobile femtosecond-terawatt laser and detection system," The European Physical Journal - Applied Physics **20**, 183–190 (2002).
20. G. Méchain, C.D'Amico, Y.-B. André, S. Tzortzakis, M. Franco, B. Prade, A. Mysyrowicz, A. Couairon, E. Salmon, and R. Sauerbrey, "Range of plasma filaments created in air by a multi-terawatt femtosecond laser," Opt. Commun. **247**, 171–180 (2005).
21. M. H. Helle, G. DiComo, S. Gregory, A. Mamonau, D. Kaganovich, R. Fischer, J. Palastro, S. Melis, and J. Peñano, "Beating Optical-Turbulence Limits Using High-Peak-Power Lasers," Phys. Rev. Appl. **12**, 054043 (2019).
22. S. Henin, Y. Petit, J. Kasparian, J.-P. Wolf, A. Jochmann, S. D. Kraft, S. Bock, U. Schramm, R. Sauerbrey, W. M. Nakaema, K. Stelmaszczyk, P. Rohwetter, L. Wöste, C.-L. Soulez, S. Mauger, L. Bergé, and S. Skupin, "Saturation of the filament density of ultrashort intense laser pulses in air," Appl. Phys. B **100**, 77–84 (2010).
23. V. P. Kandidov, N. Akozbek, M. Scalora, O. G. Kosareva, A. V. Nyakk, Q. Luo, S. A. Hosseini, and S. L. Chin, "A method for spatial regularisation of a bunch of filaments in a femtosecond laser pulse," Quantum Electron. **34**, 879 (2004).
24. E. Mitina, D. Uryupina, N. Zhidovtsev, R. Volkov, O. Kosareva, and A. Savel'ev, "Long-range robust multifilament arrays from terawatt femtosecond beam," Laser Phys. Lett. **19**, 015201 (2021).
25. S. Tochitsky, E. Welch, M. Polyanskiy, I. Pogorelsky, P. Panagiotopoulos, M. Kolesik, E. M. Wright, S. W. Koch, J. V. Moloney, J. Pigeon, and C. Joshi, "Megafilament in air formed by self-guided terawatt long-wavelength infrared laser," Nat. Photonics **13**, 41–46 (2019).
26. O. G. Kosareva, V. P. Kandidov, A. Brodeur, C. Y. Chien, and S. L. Chin, "Conical emission from laser–plasma interactions in the filamentation of powerful ultrashort laser pulses in air," Opt. Lett. **22**, 1332–1334 (1997).
27. K. Y. Kim, I. Alexeev, and H. M. Milchberg, "Single-shot supercontinuum spectral interferometry," Appl. Phys. Lett. **81**, 4124–4126 (2002).
28. J. H. Sung, J. Y. Park, T. Imran, Y. S. Lee, and C. H. Nam, "Generation of 0.2-TW 5.5-fs optical pulses at 1 kHz using a differentially pumped hollow-fiber chirped-mirror compressor," Appl. Phys. B **82**, 5–8 (2006).
29. P. He, Y. Liu, K. Zhao, H. Teng, X. He, P. Huang, H. Huang, S. Zhong, Y. Jiang, S. Fang, X. Hou, and Z. Wei, "High-efficiency supercontinuum generation in solid thin plates at 0.1 TW level," Opt. Lett. **42**, 474–477 (2017).

30. F. Salehi, M. Le, L. Railing, M. Kolesik, and H. M. Milchberg, "Laser-Accelerated, Low-Divergence 15-MeV Quasimonoenergetic Electron Bunches at 1 kHz," Phys. Rev. X **11**, 021055 (2021).
31. F. Théberge, W. Liu, P. Tr. Simard, A. Becker, and S. L. Chin, "Plasma density inside a femtosecond laser filament in air: Strong dependence on external focusing," Phys. Rev. E **74**, 036406 (2006).
32. D. Reyes, M. Baudelet, M. Richardson, and S. Rostami Fairchild, "Transition from linear- to nonlinear-focusing regime of laser filament plasma dynamics," J. Appl. Phys. **124**, 053103 (2018).
33. Y.-H. Chen, S. Varma, T. M. Antonsen, and H. M. Milchberg, "Direct Measurement of the Electron Density of Extended Femtosecond Laser Pulse-Induced Filaments," Phys. Rev. Lett. **105**, 215005 (2010).
34. S. L. Chin, D. K. Evans, R. D. McAlpine, and W. N. Selander, "Single-pulse photoacoustic technique for measuring IR multiphoton absorption by polyatomic molecules," Appl. Opt. **21**, 65–68 (1982).
35. A. Couairon, E. Brambilla, T. Corti, D. Majus, O. de J. Ramírez-Góngora, and M. Kolesik, "Practitioner's guide to laser pulse propagation models and simulation," Eur. Phys. J. Spec. Top. **199**, 5–76 (2011).
36. M. Kolesik, M. Kolesik, P. Panagiotopoulos, P. Panagiotopoulos, J. V. Moloney, and J. V. Moloney, "Nonlinear localization of high energy long wave laser pulses in fully correlated 3D turbulence," Opt. Lett. **47**, 1782–1785 (2022).
37. J. Papeer, D. Gordon, P. Sprangle, M. Botton, and A. Zigler, "Temporal evolution of femtosecond laser induced plasma filament in air and N2," Appl. Phys. Lett. **103**, 244102 (2013).
38. J. Peñano, B. Hafizi, A. Ting, and M. Helle, "Theoretical and numerical investigation of filament onset distance in atmospheric turbulence," J. Opt. Soc. Am. B **31**, 963–971 (2014).
39. L. B. Stotts, J. R. Peñano, J. A. Tellez, J. D. Schmidt, and V. J. Urick, "Engineering equations for the filamentation collapse distance in lossy, turbulent, nonlinear media," Opt. Express **27**, 25126–25141 (2019).
40. Ph. Rohwetter, K. Stelmaszczyk, L. Wöste, R. Ackermann, G. Méjean, E. Salmon, J. Kasparian, J. Yu, and J.-P. Wolf, "Filament-induced remote surface ablation for long range laser-induced breakdown spectroscopy operation," Spectrochimica Acta Part B: Atomic Spectroscopy **60**, 1025–1033 (2005).
41. T. Produit, P. Walch, C. Herkommer, A. Mostajabi, M. Moret, U. Andral, A. Sunjerga, M. Azadifar, Y.-B. André, B. Mahieu, W. Haas, B. Esmiller, G. Fournier, P. Krötz, T. Metzger, K. Michel, A. Mysyrowicz, M. Rubinstein, F. Rachidi, J. Kasparian, J.-P. Wolf, and A. Houard, "The laser lightning rod project," Eur. Phys. J. Appl. Phys. **93**, 10504 (2021).
42. J. K. Wahlstrand, S. Zahedpour, Y.-H. Cheng, J. P. Palastro, and H. M. Milchberg, "Absolute measurement of the ultrafast nonlinear electronic and rovibrational response in H_2 and D_2," Phys. Rev. A **92**, 063828 (2015).
43. Y. Chen, "The ultrafast nonlinear response of air molecules and its effect on femtosecond laser plasma filaments in atmosphere," Ph.D., University of Maryland, College Park (2011).

44. Y.-H. Chen, S. Varma, A. York, and H. M. Milchberg, "Single-shot, space- and time-resolved measurement of rotational wavepacket revivals in H_2, D_2, N_2, O_2, and N_2O," Opt. Express **15**, 11341–11357 (2007).
45. J. K. Wahlstrand, S. Zahedpour, A. Bahl, M. Kolesik, and H. M. Milchberg, "Bound-Electron Nonlinearity Beyond the Ionization Threshold," Phys. Rev. Lett. **120**, 183901 (2018).
46. A. Schmitt-Sody, H. G. Kurz, L. Bergé, S. Skupin, and P. Polynkin, "Picosecond laser filamentation in air," New J. Phys. **18**, 093005 (2016).
47. R. G. Tonkyn, J. W. Winniczek, and M. G. White, "Rotationally resolved photoionization of O2+ near threshold," Chem. Phys. Lett. **164**, 137–142 (1989).
48. L. V. Keldysh and Lebedev, P. N., "Ionization in the field of a strong electromagnetic wave," Soviet Physics-JETP **20**, 1307–1314 (1965).
49. J. K. Wahlstrand, Y.-H. Cheng, and H. M. Milchberg, "Absolute measurement of the transient optical nonlinearity in N_2, O_2, N_2O, and Ar," Phys. Rev. A **85**, 043820 (2012).
50. Y.-H. Cheng, J. K. Wahlstrand, N. Jhajj, and H. M. Milchberg, "The effect of long timescale gas dynamics on femtosecond filamentation," Opt. Express **21**, 4740–4751 (2013).
51. F. Salehi, A. J. Goers, G. A. Hine, L. Feder, D. Kuk, B. Miao, D. Woodbury, K. Y. Kim, and H. M. Milchberg, "MeV electron acceleration at 1 kHz with <10mJ laser pulses," Opt. Lett. **42**, 215–218 (2017).
52. G. Méjean, J. Kasparian, E. Salmon, J. Yu, J.-P. Wolf, R. Bourayou, R. Sauerbrey, M. Rodriguez, L. Wöste, H. Lehmann, B. Stecklum, U. Laux, J. Eislöffel, A. Scholz, and A. P. Hatzes, "Towards a supercontinuum-based infrared lidar," Appl. Phys. B **77**, 357–359 (2003).
53. S. L. Chin, A. Talebpour, J. Yang, S. Petit, V. P. Kandidov, O. G. Kosareva, and M. P. Tamarov, "Filamentation of femtosecond laser pulses in turbulent air," Appl Phys B **74**, 67–76 (2002).
54. V. P. Kandidov, O. G. Kosareva, M. P. Tamarov, A. Brodeur, and S. L. Chin, "Nucleation and random movement of filaments in the propagation of high-power laser radiation in a turbulent atmosphere," Quantum Electron. **29**, 911 (1999).
55. A. Houard, M. Franco, B. Prade, A. Durécu, L. Lombard, P. Bourdon, O. Vasseur, B. Fleury, C. Robert, V. Michau, A. Couairon, and A. Mysyrowicz, "Femtosecond filamentation in turbulent air," Phys. Rev. A **78**, 033804 (2008).
56. W. Liu, F. Théberge, E. Arévalo, J.-F. Gravel, A. Becker, and S. L. Chin, "Experiment and simulations on the energy reservoir effect in femtosecond light filaments," Opt. Lett. **30**, 2602–2604 (2005).
57. E. T. J. Nibbering, G. Grillon, M. A. Franco, B. S. Prade, and A. Mysyrowicz, "Determination of the inertial contribution to the nonlinear refractive index of air, N_2, and O_2 by use of unfocused high-intensity femtosecond laser pulses," J. Opt. Soc. Am. B **14**, 650–660 (1997).
58. D. S. Uryupina, A. S. Bychkov, D. V. Pushkarev, E. V. Mitina, A. B. Savel'ev, O. G. Kosareva, N. A. Panov, A. A. Karabutov, and E. B. Cherepetskaya,

"Laser optoacoustic diagnostics of femtosecond filaments in air using wideband piezoelectric transducers," Laser Phys. Lett. **13**, 095401 (2016).
59. N. Jhajj, I. Larkin, E. W. Rosenthal, S. Zahedpour, J. K. Wahlstrand, and H. M. Milchberg, "Spatiotemporal Optical Vortices," Phys. Rev. X **6**, 031037 (2016).
60. F. Théberge, J.-F. Daigle, J.-C. Kieffer, F. Vidal, and M. Châteauneuf, "Laser-guided energetic discharges over large air gaps by electric-field enhanced plasma filaments," Sci. Rep. **7**, 40063 (2017).
61. P. B. Corkum, C. Rolland, and T. Srinivasan-Rao, "Supercontinuum Generation in Gases," Phys. Rev. Lett. **57**, 2268–2271 (1986).
62. A. Englesbe, J. Elle, R. Reid, A. Lucero, H. Pohle, M. Domonkos, S. Kalmykov, K. Krushelnick, and A. Schmitt-Sody, "Gas pressure dependence of microwave pulses generated by laser-produced filament plasmas," Opt. Lett. **43**, 4953–4956 (2018).
63. S. Tzortzakis, B. Prade, M. Franco, and A. Mysyrowicz, "Time-evolution of the plasma channel at the trail of a self-guided IR femtosecond laser pulse in air," Opt. Commun. **181**, 123–127 (2000).
64. F. Vidal, D. Comtois, C.-Y. Chien, A. Desparois, B. La Fontaine, T. W. Johnston, J.-C. Kieffer, H. P. Mercure, H. Pepin, and F. A. Rizk, "Modeling the triggering of streamers in air by ultrashort laser pulses," IEEE Transactions on Plasma Science **28**, 418–433 (2000).
65. J. H. Churnside and R. J. Lataitis, "Wander of an optical beam in the turbulent atmosphere," Appl. Opt. **29**, 926–930 (1990).
66. M. Kolesik and J. V. Moloney, "Nonlinear optical pulse propagation simulation: From Maxwell's to unidirectional equations," Phys. Rev. E **70**, 036604 (2004).
67. D. Jang, R. M. Schwartz, D. Woodbury, J. Griff-McMahon, A. H. Younis, H. M. Milchberg, and K.-Y. Kim, "Efficient terahertz and Brunel harmonic generation from air plasma via mid-infrared coherent control," Optica **6**, 1338–1341 (2019).
68. C. Macaskill and T. Ewart, "Computer Simulation of Two-dimensional Random Wave Propagation," IMA Journal of Applied Mathematics **33**, (1984).
69. G. Paunescu, G. Spindler, W. Riede, H. Schröder, and A. Giesen, "Multifilamentation of femtosecond laser pulses induced by small-scale air turbulence," Appl. Phys. B **96**, 175 (2009).
70. S. A. Shlenov and A. I. Markov, "Control of filamentation of femtosecond laser pulses in a turbulent atmosphere," Quantum Electron. **39**, 658 (2009).
71. A. H. Guenther and J. R. Bettis, "A review of laser-triggered switching," Proceedings of the IEEE **59**, 689–697 (1971).
72. W. K. Pendleton and A. H. Guenther, "Investigation of a Laser Triggered Spark Gap," Rev. Sci. Instrum. **36**, 1546–1550 (1965).
73. A. Guenther and J. Bettis, "12.2 - Laser-triggered megavolt switching," IEEE J. Quantum Electron. **3**, 581–588 (1967).
74. L. L. Steinmetz, "Laser-Triggered Spark Gap," Rev. Sci. Instrum. **39**, 904–909 (1968).
75. M. J. Kushner, R. D. Milroy, and W. D. Kimura, "A laser-triggered spark gap model," J. Appl. Phys. **58**, 2988–3000 (1985).

76. L. B. Loeb and A. F. Kip, "Electrical Discharges in Air at Atmospheric Pressure The Nature of the Positive and Negative Point-to-Plane Coronas and the Mechanism of Spark Propagation," J. Appl. Phys. **10**, 142–160 (1939).
77. L. B. Loeb and J. M. Meek, "The Mechanism of Spark Discharge in Air at Atmospheric Pressure. I," J. Appl. Phys. **11**, 438–447 (1940).
78. L. B. Loeb and J. M. Meek, "The Mechanism of Spark Discharge in Air at Atmospheric Pressure. II," J. Appl. Phys. **11**, 459–474 (1940).
79. J. M. Meek, "A Theory of Spark Discharge," Phys. Rev. **57**, 722–728 (1940).
80. J. S. Townsend, "The Conductivity produced in Gases by the Motion of Negatively-charged Ions," Nature **62**, 340–341 (1900).
81. M. Miki, Y. Aihara, and T. Shindo, "Development of long gap discharges guided by a pulsed CO_2 laser," J. Phys. D **26**, 1244–1252 (1993).
82. P. Polynkin, B. Pasenhow, N. Driscoll, M. Scheller, E. M. Wright, and J. V. Moloney, "Seeded optically driven avalanche ionization in molecular and noble gases," Phys. Rev. A **86**, 043410 (2012).
83. L. Bergé, S. Skupin, R. Nuter, J. Kasparian, and J.-P. Wolf, "Ultrashort filaments of light in weakly ionized, optically transparent media," Rep. Prog. Phys. **70**, 1633–1713 (2007).
84. P. Polynkin and J. V. Moloney, "Optical breakdown of air triggered by femtosecond laser filaments," Appl. Phys. Lett. **99**, 151103 (2011).
85. M. Rodriguez, R. Sauerbrey, H. Wille, L. Wöste, T. Fujii, Y.-B. André, A. Mysyrowicz, L. Klingbeil, K. Rethmeier, W. Kalkner, J. Kasparian, E. Salmon, J. Yu, and J.-P. Wolf, "Triggering and guiding megavolt discharges by use of laser-induced ionized filaments," Opt. Lett. **27**, 772–774 (2002).
86. K. A. Saum and D. W. Koopman, "Discharges Guided by Laser-Induced Rarefaction Channels," The Physics of Fluids **15**, 2077–2079 (1972).
87. A. Schmitt-Sody, D. French, W. White, A. Lucero, W. P. Roach, and V. Hasson, "The importance of corona generation and leader formation during laser filament guided discharges in air," Appl. Phys. Lett. **106**, 124101 (2015).
88. S. Tzortzakis, B. Prade, M. Franco, A. Mysyrowicz, S. Hüller, and P. Mora, "Femtosecond laser-guided electric discharge in air," Phys. Rev. E **64**, 057401 (2001).
89. F. Paschen, "On the potential difference required for spark initiation in air, hydrogen, and carbon dioxide at different pressures," Annalen der Physik **273**, 69–75 (1889).
90. G. Point, L. Arantchouk, E. Thouin, J. Carbonnel, A. Mysyrowicz, and A. Houard, "Long-lived laser-induced arc discharges for energy channeling applications," Sci. Rep. **7**, 13801 (2017).
91. G. Point, L. Arantchouk, J. Carbonnel, A. Mysyrowicz, and A. Houard, "Plasma dynamics of a laser filamentation-guided spark," Phys. Plasmas **23**, 093505 (2016).
92. Y. Brelet, A. Houard, G. Point, B. Prade, L. Arantchouk, J. Carbonnel, Y.-B. André, M. Pellet, and A. Mysyrowicz, "Radiofrequency plasma antenna generated by femtosecond laser filaments in air," Appl. Phys. Lett. **101**, 264106 (2012).

93. X. M. Zhao, J.-C. Diels, C. Y. Wang, and J. M. Elizondo, "Femtosecond ultraviolet laser pulse induced lightning discharges in gases," IEEE Journal of Quantum Electronics **31**, 599–612 (1995).
94. J. Kasparian, R. Ackermann, Y.-B. André, G. Méchain, G. Méjean, B. Prade, P. Rohwetter, E. Salmon, K. Stelmaszczyk, J. Yu, A. Mysyrowicz, R. Sauerbrey, L. Wöste, and J.-P. Wolf, "Electric events synchronized with laser filaments in thunderclouds," Opt. Express **16**, 5757–5763 (2008).
95. D. Comtois, C. Y. Chien, A. Desparois, F. Génin, G. Jarry, T. W. Johnston, J.-C. Kieffer, B. La Fontaine, F. Martin, R. Mawassi, H. Pépin, F. a. M. Rizk, F. Vidal, P. Couture, H. P. Mercure, C. Potvin, A. Bondiou-Clergerie, and I. Gallimberti, "Triggering and guiding leader discharges using a plasma channel created by an ultrashort laser pulse," Appl. Phys. Lett. **76**, 819–821 (2000).
96. T. Fujii, M. Miki, N. Goto, A. Zhidkov, T. Fukuchi, Y. Oishi, and K. Nemoto, "Leader effects on femtosecond-laser-filament-triggered discharges," Phys. Plasmas **15**, 013107 (2008).
97. K. Sugiyama, T. Fujii, M. Miki, A. Zhidkov, M. Yamaguchi, E. Hotta, and K. Nemoto, "Submicrosecond laser-filament-assisted corona bursts near a high-voltage electrode," Phys. Plasmas **17**, 043108 (2010).
98. D. F. Gordon, A. Ting, R. F. Hubbard, E. Briscoe, C. Manka, S. P. Slinker, A. P. Baronavski, H. D. Ladouceur, P. W. Grounds, and P. G. Girardi, "Streamerless guided electric discharges triggered by femtosecond laser filaments," Phys. Plasmas **10**, 4530–4538 (2003).
99. A. Schmitt-Sody, J. Elle, A. Lucero, M. Domonkos, A. Ting, and V. Hasson, "Dependence of single-shot pulse durations on near-infrared filamentation-guided breakdown in air," AIP Adv. **7**, 035018 (2017).
100. C. W. Siders, J. L. W. Siders, A. J. Taylor, S.-G. Park, and A. M. Weiner, "Efficient high-energy pulse-train generation using a 2^n-pulse michelson interferometer," Appl. Opt. **37**, 5302–5305 (1998).
101. S. Tzortzakis, M. A. Franco, Y.-B. André, A. Chiron, B. Lamouroux, B. S. Prade, and A. Mysyrowicz, "Formation of a conducting channel in air by self-guided femtosecond laser pulses," Phys. Rev. E **60**, R3505–R3507 (1999).
102. Y. Itikawa, "Cross Sections for Electron Collisions with Nitrogen Molecules," J. Phys. Chem. Ref. Data **35**, 31–53 (2006).
103. Y. Itikawa, "Cross Sections for Electron Collisions with Oxygen Molecules," J. Phys. Chem. Ref. Data **38**, 1–20 (2009).
104. Y. S. Touloukian, P. E. Liley, and S. C. Saxena, "Thermal Conductivity–Nonmetalic Liquids and Gasses," Thermophysical Properties of Matter **3**, 512 (1970).
105. V. D. Zvorykin, S. A. Goncharov, A. A. Ionin, D. V. Mokrousova, S. V. Ryabchuk, L. V. Seleznev, I. V. Smetanin, A. V. Shutov, E. S. Sunchugasheva, and N. N. Ustinovskii, "Arrangement of multiple UV filaments by periodic amplitude masks," Nuclear Instruments and Methods in Physics Research Section B: Beam Interactions with Materials and Atoms **402**, 331–335 (2017).
106. D. V. Pushkarev, D. V. Pushkarev, D. V. Pushkarev, A. S. Lar'kin, E. V. Mitina, N. A. Zhidovtsev, D. S. Uryupina, D. S. Uryupina, R. V. Volkov, S. V. Karpeev, S. V. Karpeev, S. N. Khonina, S. N. Khonina, A. A. Karabutov, Y. E.

Geints, O. G. Kosareva, O. G. Kosareva, A. B. Savel'ev, and A. B. Savel'ev, "Robust multifilament arrays in air by Dammann grating," Opt. Express **29**, 34189–34204 (2021).
107. A. Vinçotte and L. Bergé, "Femtosecond Optical Vortices in Air," Phys. Rev. Lett. **95**, 193901 (2005).
108. L. T. Vuong, T. D. Grow, A. Ishaaya, A. L. Gaeta, G. W. 't Hooft, E. R. Eliel, and G. Fibich, "Collapse of Optical Vortices," Phys. Rev. Lett. **96**, 133901 (2006).
109. E. Treacy, "Optical pulse compression with diffraction gratings," IEEE J. Quantum Electron. **5**, 454–458 (1969).
110. G. Méchain, A. Couairon, M. Franco, B. Prade, and A. Mysyrowicz, "Organizing Multiple Femtosecond Filaments in Air," Phys. Rev. Lett. **93**, 035003 (2004).
111. A. Ryabtsev, S. Pouya, M. Koochesfahani, and M. Dantus, "Vortices in the wake of a femtosecond laser filament," Opt. Express **22**, 26098–26102 (2014).
112. G. J. Mullaney, W. H. Christiansen, and D. A. Russell, "Fog dissipation using a co2 laser," Appl. Phys. Lett. **13**, 145–147 (1968).
113. F. Courvoisier, V. Boutou, J. Kasparian, E. Salmon, G. Méjean, J. Yu, and J.-P. Wolf, "Ultraintense light filaments transmitted through clouds," Appl. Phys. Lett. **83**, 213–215 (2003).
114. M. C. Schroeder, I. Larkin, T. Produit, E. W. Rosenthal, H. Milchberg, and J.-P. Wolf, "Molecular quantum wakes for clearing fog," Opt. Express **28**, 11463–11471 (2020).
115. A. Goffin, J. Griff-McMahon, I. Larkin, and H. M. Milchberg, "Atmospheric aerosol clearing by femtosecond filaments," Phys. Rev. Appl. (accepted).
116. A. Couairon and L. Bergé, "Light Filaments in Air for Ultraviolet and Infrared Wavelengths," Phys. Rev. Lett. **88**, 135003 (2002).
117. O. Lahav, L. Levi, I. Orr, R. A. Nemirovsky, J. Nemirovsky, I. Kaminer, M. Segev, and O. Cohen, "Long-lived waveguides and sound-wave generation by laser filamentation," Phys. Rev. A **90**, 021801 (2014).
118. G. Point, C. Milián, A. Couairon, A. Mysyrowicz, and A. Houard, "Generation of long-lived underdense channels using femtosecond filamentation in air," J. Phys. B **48**, 094009 (2015).
119. J. Yu, D. Mondelain, J. Kasparian, E. Salmon, S. Geffroy, C. Favre, V. Boutou, and J.-P. Wolf, "Sonographic probing of laser filaments in air," Appl. Opt. **42**, 7117–7120 (2003).
120. G. Schimmel, T. Produit, D. Mongin, J. Kasparian, and J.-P. Wolf, "Free space laser telecommunication through fog," Optica **5**, 1338–1341 (2018).
121. L. de la Cruz, E. Schubert, D. Mongin, S. Klingebiel, M. Schultze, T. Metzger, K. Michel, J. Kasparian, and J.-P. Wolf, "High repetition rate ultrashort laser cuts a path through fog," Appl. Phys. Lett. **109**, 251105 (2016).
122. B. A. Kunkel, "Fog Drop-Size Distributions Measured with a Laser Hologram Camera," Journal of Applied Meteorology and Climatology **10**, 482–486 (1971).

123. S. Skupin, L. Bergé, U. Peschel, and F. Lederer, "Interaction of Femtosecond Light Filaments with Obscurants in Aerosols," Phys. Rev. Lett. **93**, 023901 (2004).
124. M. Kolesik and J. V. Moloney, "Self-healing femtosecond light filaments," Opt. Lett. **29**, 590–592 (2004).